

AD-A112 274

AIR FORCE GEOPHYSICS LAB HANSCOM AFB MA
TEMPORAL AND SPATIAL STRUCTURE OF SHORT WAVELENGTH INFRARED AUR--ETC(U)
OCT 81 E R HUPPI, D VILLANUCCI, M BRUCE

F/6 4/1

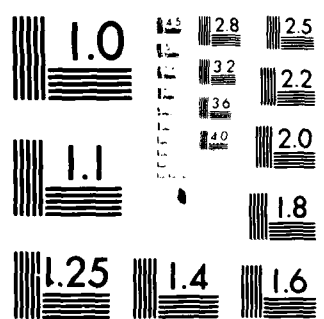
UNCLASSIFIED

AFGL-TR-81-0299

NL

[redacted]
[redacted]

END
DATE FILMED
4-82
DTIC



MICROCOPY RESOLUTION TEST CHART
NATIONAL BUREAU OF STANDARDS 1964 A

ADA112274

AFGL-TR-81-0299
ENVIRONMENTAL RESEARCH PAPERS, NO. 756



(12)

Temporal and Spatial Structure of Short Wavelength Infrared Auroral Backgrounds

E. RAY HUPPI
DENNIS VILLANUCCI
MARSHALL BRUCE

13 October 1981

DTIC FILE COPY

Approved for public release; distribution unlimited.

DTIC
SELECTED
MAR 22 1982

OPTICAL PHYSICS DIVISION
AIR FORCE GEOPHYSICS LABORATORY
PROJECT 7670
HANSCOM AFB, MASSACHUSETTS 01731

AIR FORCE SYSTEMS COMMAND, USAF



82 03 22 130

This report has been reviewed by the ESD Public Affairs Office (PA)
and is releasable to the National Technical Information Service (NTIS).

This technical report has been reviewed and
is approved for publication.

Alva T. Stair, Jr.

DR. ALVA T. STAIR, Jr.
Chief Scientist

Qualified requestors may obtain additional copies from the
Defense Technical Information Center. All others should apply
to the National Technical Information Service.

Unclassified

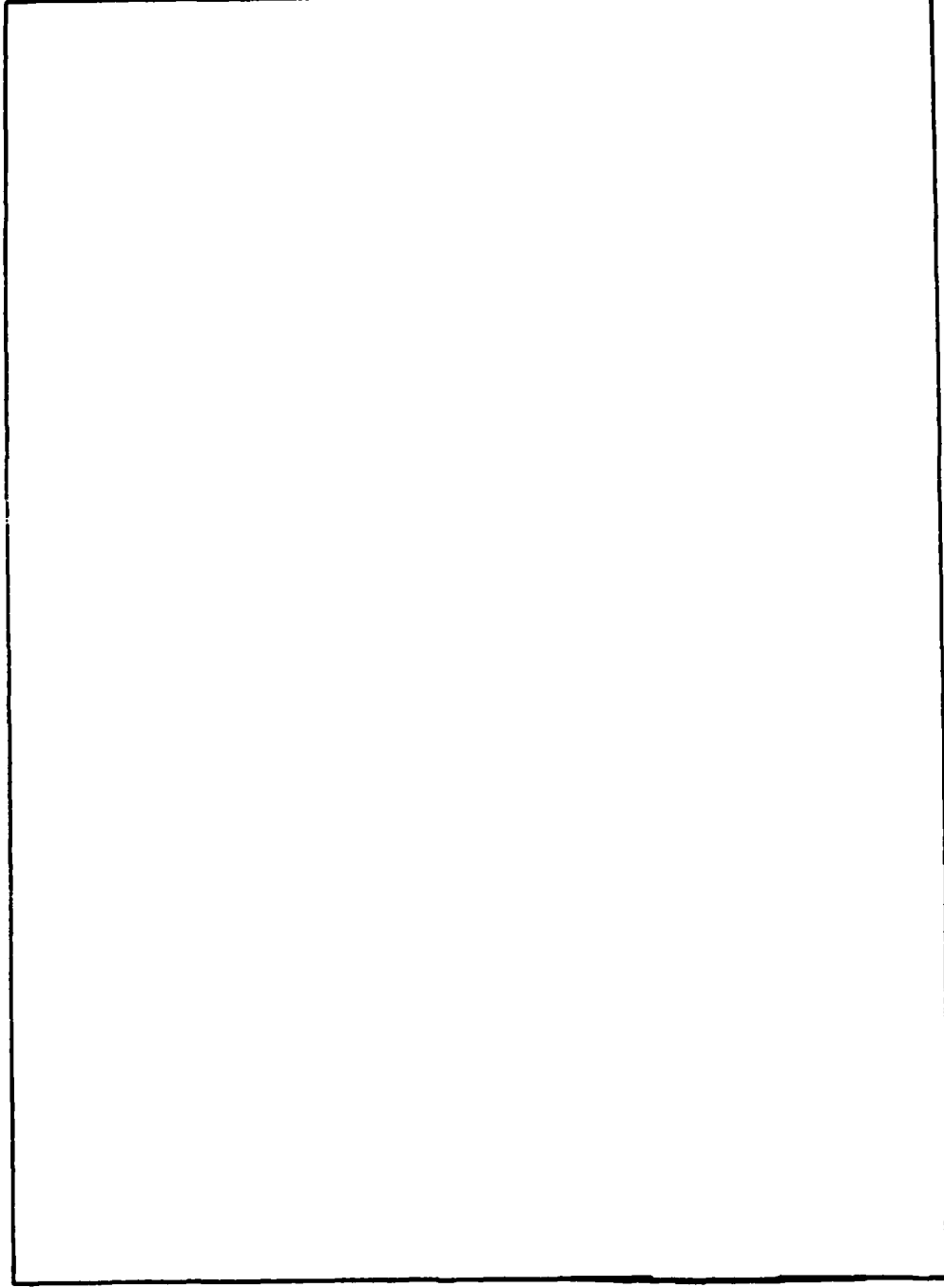
SECURITY CLASSIFICATION OF THIS PAGE (When Data Entered)

DD FORM 1 JUN 73 1473

Unclassified

SECURITY CLASSIFICATION OF THIS PAGE (When Data Entered)

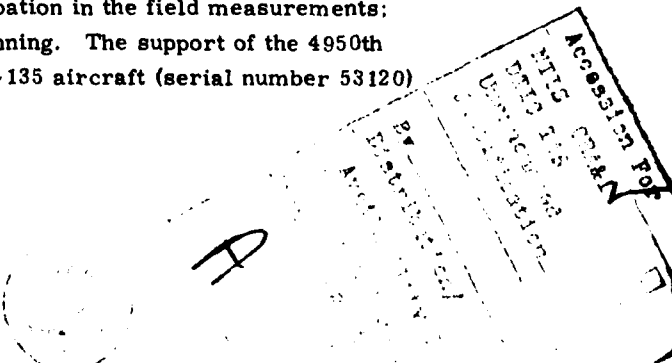
SECURITY CLASSIFICATION OF THIS PAGE(When Data Entered)

A large, empty rectangular box with a black border, occupying most of the page below the classification header. It appears to be a redaction or a placeholder for sensitive information.

SECURITY CLASSIFICATION OF THIS PAGE(When Data Entered)

Preface

The authors acknowledge the continued support and scientific guidance of Dr. A. T. Stair, Jr., Branch Chief, Radiation Effects Branch, Optical Physics Division, Air Force Geophysics Laboratory, who initially planned this auroral measurements experiment. The continued interest and scientific collaboration of Dr. I. L. Kofsky of PhotoMetrics, Inc. is also acknowledged. This effort was supported by the Defense Nuclear Agency, and their support, and particularly the support of DNA project officers Maj. James Mayo and Lt. Col. William McKechnie, is gratefully acknowledged. A significant group of scientists, engineers and technicians contributed to the development of the optical instrumentation, the field measurement effort, and the data reduction and analysis. The authors thank the personnel of PhotoMetrics, Inc., Visidyne, Inc., Stanford Research Institute, Stewart Radiance Laboratory and Electro-Dynamics Laboratories of Utah State University, Geophysical Institute of the University of Alaska, and Air Force Geophysics Laboratory for their support. In particular, the authors recognize the contribution of Randy Sluder, PhotoMetrics, Inc., for his efforts in developing the low light level television; John Kemp, Ronald Huppi, Don Goode, Charles Eastman, and Thomas Hudson of Stewart Radiance Laboratory for instrumentation development, participation in the field measurements, and data reduction; John LaSpina, David Newell, and Robert Pierce of AFGL for their efforts in instrumentation development, calibration, and participation in the field measurements; and John Reed of Visidyne, Inc. for mission planning. The support of the 4950th Test Wing in operating and maintaining the NKC-135 aircraft (serial number 53120) is also acknowledged.



Contents

1. INTRODUCTION	9
2. INSTRUMENTATION	13
2.1 SWIR Radiometer	14
2.2 Narrow Field Photometer	16
2.3 Low Light Level Television	18
3. DATA ANALYSIS	18
3.1 Chemiluminous Yields and Delay Compared with Solar Illumination, Auroral Altitude and Magnetic Index	19
3.2 3 μ m and 5577A Time Response and Yield Efficiency Using Fourier Transform Technique	32
4. CONCLUSIONS	51
REFERENCES	55
APPENDIX A: Data Samples	57
DISTRIBUTION LIST	91

Illustrations

1. Comparison of Fields of View of NKC-135 A/55-3120's Photometers and Radiometers in Earlier, and in 1979-80 Measurements of SWIR Emission Structure	11
2. Spectral Response (a) SWIR Radiometer and (b) NIR Radiometer	16

Illustrations

3. 3914/5577 Photometer Spectral Response (a) 3914 \AA Channel, (b) 5577 \AA Channel	17
4. Cross-plots of 2.8-3 μm and 3914 \AA Band Intensities Measured by the Narrow-field Instruments at Three Different Solar Depression Angles Representing (a) 0 Percent (Case 1), (b) 53 Percent (Case 3), and (c) 100 Percent (Case 12) Fractional Illumination	24
5. Average NO Overtone Yield Compared with (a) Average 3914 \AA Intensity, (b) Fractional Auroral Illumination, (c) Hydroxyl Fundamental/Overtone Ratio, and (d) Global Magnetic Index for the 15 Data Segments in Table 3	27
6. Average NO Overtone Yield for the 15 Data Segments Compared with Altitude of Peak Energy Deposition	28
7. Instantaneous Ratio (SWIR/3914 \AA Photon) Plotted Against In- stantaneous Peak Energy Deposition Altitude for Flight 026 (Case 13, 1159:30 - 1202:53), and Compared with Simple Calculation of Expected Altitude Dependence	29
8. Apparent SWIR Delay Compared with (a) Fractional Auroral Illumination and (b) Peak Energy Deposition Altitude for the 15 Data Segments	31
9. 3 μm Auroral Emission Measured 2:13:57 GMT, 27 April 1979, Flight 909, Case 3 With Fourier Transforms	33
10. 3914 \AA Signal and Corresponding Complex Fourier Transform of Data Measured 2:13:57 GMT, 27 April 1979, Flight 909, Case 3	34
11. 5577 \AA Signal and Corresponding Complex Fourier Transform of Data Measured 2:13:57 GMT, 27 April 1979, Flight 909, Case 3	35
12. Complex Transfer Function (Unfiltered, Upper; Filtered, Lower) of 3 μm Response on 27 April 1979	37
13. Complex Transfer Function (Unfiltered, Upper; Filtered, Lower) of 5577 \AA Response on 27 April 1979	38
14. The Rate Equations in Matrix Form	47
15. NO Overtone Photons per N(^2D) + O ₂ Reaction	52
16. NO Fundamental Photons per N(^2D) + O ₂ Reaction	53
A1. Case 1, Flight 907, 23 April 1979	60
A2. All-Sky Photographs for Case 1, Flight 907, 23 April 1979	61
A3. Case 2, Flight 909, 27 April 1979	62
A4. All-Sky Photographs for Case 2, Flight 909, 27 April 1979	63
A5. Case 3, Flight 909, 27 April 1979	64
A6. All-Sky Photographs for Case 3, Flight 909, 27 April 1979	65
A7. Case 4, Flight 909, 27 April 1979	66
A8. All-Sky Photographs for Case 4, Flight 909, 27 April 1979	67
A9. Case 5, Flight 909, 27 April 1979	68

Illustrations

A10. All-Sky Photographs for Case 5, Flight 909, 27 April 1979	69
A11. Case 6, Flight 908, 25 April 1979	70
A12. All-Sky Photographs for Case 6, Flight 908, 25 April 1979	71
A13. Case 7, Flight 924, 18 September 1979	72
A14. All-Sky Photographs for Case 7, Flight 924, 18 September 1979	73
A15. Case 8, Flight 926, 25 September 1979	74
A16. All-Sky Photographs for Case 8, Flight 926, 25 September 1979	75
A17. Case 9, Flight 927, 27 September 1979	76
A18. All-Sky Photographs for Case 9, Flight 927, 27 September 1979	77
A19. Case 11, Flight 023, 7 August 1980	78
A20. All-Sky Photographs for Case 11, Flight 023, 7 August 1980	79
A21. Case 12, Flight 026, 18 August 1980	80
A22. All-Sky Photographs for Case 12, Flight 026, 18 August 1980	80
A23. Case 13, Flight 026, 18 August 1980	81
A24. All-Sky Photographs for Case 13, Flight 026, 18 August 1980	82
A25. Case 14, Flight 027, 19 August 1980	83
A26. All-Sky Photographs for Case 14, Flight 027, 19 August 1980	84
A27. Case 15A, Flight 027, 19 August 1980	85
A28. All-Sky Photographs for Case 15A, Flight 027, 19 August 1980	86
A29. Case 15B, Flight 027, 19 August 1980	87
A30. All-Sky Photographs for Case 15B, Flight 027, 19 August 1980	88

Tables

1. Instrument Characteristics	15
2. Instrument Responsivity	18
3. Auroral and Observation Parameters During SWIR Enhancements	20
4. Fractional Illumination of Aurora for the 15 Data Segments Identified by Case Number	22

Tables

5. Chemiluminous Yields and Apparent SWIR Delays Derived From the 15 Data Segments Listed Compared with Peak Auroral Altitude and Aircraft Heading	26
6. Correlation of SWIR Enhancement Delay with Several Auroral and Measurement Parameters	30
7. Photon Ratios and Quenching Coefficients	39
8. Einstein Emission Coefficients A_{vv}^{-1} of NO and the Relative Production for the $N(^2D) + O_2$ Reaction (Billingsley ¹⁵)	45
9. Radiative Cascade Matrix	46
10. NO Atmosphere and Filter Transmission	48
11. NO Overtone [Photons/ $N(^2D) + O_2$] Reaction Quenching Coefficient α For $NO(v) + M \rightarrow NO(0) + M$	49
12. NO Fundamental [Photons/ $N(^2D) + O_2$] Reaction Quenching Coefficient α For $NO(v) + M \rightarrow NO(0) + M$	49
13. NO Overtone [Photons/ $N(^2D) + O_2$] Reaction Quenching Coefficient α For $NO(v) + M \rightarrow NO(v-1) + M$	50
14. NO Fundamental [Photons/ $N(^2D) + O_2$] Reaction Quenching Coefficient α For $NO(v) + M \rightarrow NO(v-1) + M$	50
A1. Auroral and Observation Parameters During SWIR Enhancements	58

Temporal and Spatial Structure of Short Wavelength Infrared Auroral Backgrounds

I. INTRODUCTION

During April 1979, September 1979, and August 1980, AFGL/OPR conducted a series of measurements of short-wavelength infrared and visible emissions from the auroral particle-excited ionosphere. Observations were conducted from AFGL's Optical Flying Laboratory (USAF NKC-135A S/N 53120) during flights into the auroral zone near 70° W longitude (1979, from Pease AFB, N.H.) and 147° W (1980, Eielson AFB, Alaska). The principal goal of this program is to investigate the sources of $2.8 - 3.1 \mu\text{m}$ band emission resulting from excitation of air by energetic-particle bombardment, and to establish the spatial and temporal correlation of emission with the deposition of ionizing-particle energy in the upper atmosphere.

The stimulating source of input power is energetic (≈ 5 keV) electrons that precipitate into the upper atmosphere at high latitudes in association with magnetospheric substorms. Spatial distribution of flux and peak energy deposition altitudes of these charged particles are measured from the air fluorescence they excite at visible wavelengths, that is, the optical aurora. In particular, fluorescence in the N_2^+ First Negative (0-0) 3914\AA band, which is directly proportional to the total energy deposited in the atmosphere, is monitored by a narrow-field photometer whose optic axis has been coaligned with a SWIR radiometer having an identical

(Received for publication 8 October 1981)

field of view. These data are supported by energy distributions measured by a low light level video camera, a photographic all-sky camera and a 12-channel filter photometer from which altitude profiles of energy deposition can be determined (Appendix II of Reference 1) and altitude profiles of ionospheric electron density measured by the Chatanika radar.

The species ionized and excited by direct electron impact and by secondary processes react with ambient molecules and atoms, producing chemiluminescence that is measurable against other natural IR atmospheric emissions. The yields or chemiluminous efficiencies in emission features, and the times for buildup and decay of the infrared radiations, complement emission spectra in identifying the radiating species and the excitation/deexcitation processes.

The atmosphere above the subsonic jet aircraft's operating altitude of 35 to 39 kft is essentially transparent to downward-directed radiation between 2.8 and 3.1 μ m. A radiometer sensitive to this band and a photometer, each with 1/6 radian fields of view were pointed toward the zenith in flights through the auroral oval in 1975-1978.² In 1979 and 1980 the fields of the coaligned instruments were reduced to 0.007 radian (< 1 km laterally projected to auroral altitudes) and the integration time required to produce acceptable signal/noise ratio was lowered from 30 sec to 0.1 sec (refer to Section II for instrument specifications). The instrument configurations are compared in Figure 1.

Data from the wide-field instruments used during the 1975-1978 flights have been evaluated and interpreted in References 3 and 4. The results, which refer to air between 100 and 150 km altitude, can be summarized as follows:

- a. SWIR output follows particle-energy input to within the ~ 20 km, 3/4 min resolution of the instruments. (No lag or "smear" can be resolved with confidence in the data traces.)
- b. Yield of SWIR photons is linear with input at all column input rates observed (about 5 to 50 erg/cm²-sec).
- c. Lumped parameter-efficiency for emission of what is interpreted as the vibrational overtone of nitric oxide molecules shows statistically-significant differences among both long (1/2 hr) and short (1 min) segments of data, with values lying between 0.4 percent and 0.7 percent.

1. Kofsky, I. L., Villanucci, D. P., and Sluder, R. B. (1977) Data Reduction and Auroral Characterizations for ICECAP III, HAES Report No. 59, DNA 4220F.
2. Huppi, R. J., and Reed, J. W. (1977) Aircraft Borne Measurements of Infrared Enhancements During ICECAP 1975 and 1976, AFGL-TR-77-0232, AD A051 454.
3. Kofsky, I. L., Villanucci, D. P., and Andrus, W. S. (1978) Assessment of Rocketborne and Airborne Infrared Data, DNA 4731F.
4. Kofsky, I. L., and Villanucci, D. P. (1979) Further Assessment of Infrared Data from Aircraft and Rocket Probes, DNA 5127F.

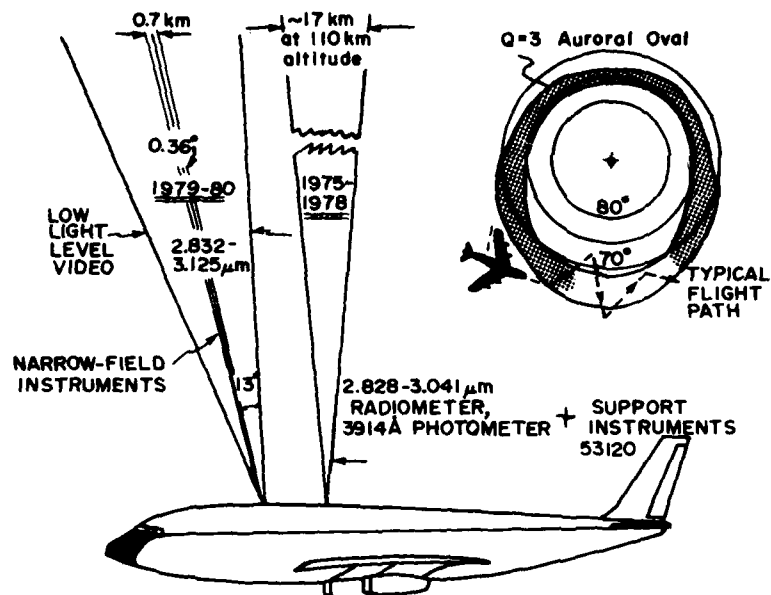


Figure 1. Comparison of Fields of View of NKC-135 A/55-3120's Photometers and Radiometers in Earlier, and in 1979-80 Measurements of SWIR Emission Structure. The diagram in the upper right illustrates the aircraft's trajectory against the rotating auroral oval (locus of most intense particle precipitation) in flight on a geomagnetic N→S→N track.

It should be noted that these aircraft results are by and large consistent with those from rocketborne radiometers, and (with the exception of the variability) with results of laboratory investigations of the radiative properties of NO.

These earlier flights also showed that both SWIR emission and the referencing visible air fluorescence can be measured when the auroral altitudes are sunlit (as reviewed in Section 5 of Reference 4). Navigating to compensate for winds and operating near the equinoxes, the aircraft is able to hold the desired solar elevation while flying within the (average) auroral oval and permitted airspace. Verification of a day-night difference in SWIR dynamics and yield would indicate a deficiency in current understanding of the processes that lead to vibrationally excited NO. No night-twilight difference in concentrations of ambient reacting species (O , O_2 , N_2) has been proposed that would have substantive effect on the reaction chain that produces NO^+ . To assess the behavior of SWIR emission during "sunlit" aurora, several transition-twilight flights were made with the narrow-field instruments in 1979 and 1980.

The narrow-angle instruments are tilted approximately 13° forward of the flying aircraft to point in the direction of the geomagnetic field when the aircraft is within the auroral oval and flying southward. In this mode they measure the emissions from regions in which the precipitating auroral electrons have a unique initial energy spectrum. Accurate co-alignment (< 3 arc min) is accomplished using a precision optical bench, the design of which is documented in Reference 5. A second, wider-field, multi-channel photometer (2° full angle) separated by approximately 43 feet from (and nominally aligned with) the prime instruments has as its major function determination of energy deposition altitudes from the photon ratios of auroral features near 6300Å and 4278Å (Appendix II of Reference 1). This information is useful in verifying the extent to which the factor of 2 variability in SWIR yield seen in earlier aircraft measurements may be correlated with emission altitude. Calculations of collisional quenching of NO⁺ by atomic oxygen (Reference 6), in fact, predict a minimum in SWIR yield near 100 km.

The determination of emission altitudes from measurements of the 6300Å and 4278Å intensities is based on the principle that this altitude is determined by variations with height of atmospheric density and composition that cause electrons of different energies to be stopped at different altitudes. Major assumptions in the theory are: (1) the optical axis of the photometer is aligned with the magnetic field; (2) steady state excitation and loss of the O(¹D) upper state, which radiates at 6300Å; and (3) a Maxwellian spectrum of the energy of the incoming electrons. The first of these is generally satisfied during segments of flights when the aircraft heading is near 180° (magnetic). In other flights, however, particularly the twilight missions where the aircraft trajectory was chosen to maintain a constant solar depression angle, this condition is not very well met. Thus, the confidence placed on altitudes derived by this method depends (at least in part) on aircraft heading.

Additionally, the assumed shape of the particle energy spectrum is a potential source of error. (The spectra measured in arcs from the various ICECAP rockets are generally poor fits to the Maxwellian model.) To this extent, the 1980 flight series was coordinated with Chatanika radar operations which directly measures altitude profiles of ionospheric electron densities.

A total of about 15 hr of coordinated measurements from 5 data missions originating at Eielson AFB were made in which the aircraft was flown along (or near) the magnetic north-south meridian through Chatanika, Alaska. Separate flight profiles were calculated for each night to obtain an adequate sampling of

-
5. Sluder, R. B., Andrus, W.S., and Kofsky, I. L. (1979) Aircraft Program for Target, Background, and Sky Radiance Measurements, AFGL-TR-79-0139, AD A076 959.
 6. Archer, D. H. (1979) Requirements for Improved Infrared Prediction Capability, HAES Report No. 78, DNA 4585F.

both sunlit and nighttime aurora. An attempt was made to synchronize the aircraft trajectories with the radar's scan rate so that the 13° tilted instrument fields would overlap the radar scan volume at 100 km.

Since the radar facility requires a preprogrammed tracking routine to attain sufficient precision for the measurements, no provision in the radar track could be made for the effects of winds on the aircraft. The aircraft was flown along a track which adjusted for the "crabbing" of the aircraft caused by winds so that the instruments would view the same region being viewed by the radar. The aircraft utilized an inertial navigation system (INS) to determine its position, but since the accumulated error of the INS from take-off to landing was as much as 3 km, the exact overlap of radar field-of-view and the airborne instrument field-of-view cannot be guaranteed.

It was decided to set up a series of checkpoints at which the aircraft would arrive "on time" in conjunction with the radar motion. No course deviations were taken from the predetermined track (about 220 km) to "chase" auroral forms, which of course lessens the probability of encountering intense particle bombardment. The number of meridian cycles completed by the radar per flight varied from 3 1/2 to 7 depending on mission duration.

There are only two positions along the track when the aircraft instruments and the radar view along the same line of sight and only one where they are viewing along the same line of sight and along the magnetic field lines, which would be the ideal condition. In the data samples analyzed, this ideal condition did not occur. The altitude of peak energy deposition obtained from the radar measurements tended to be 5 - 15 km higher than altitudes derived from the aircraft 12-channel photometer readings and were in best agreement when the altitudes obtained by the photometric method were averaged over a short section of data rather than determined only at the point of maximum auroral intensity. This is expected since the radar data was typically averaged over a 15-sec period. Radar measurements were only available for the 1980 flights from Alaska, so to standardize the results presented here, all peak energy deposition altitudes were derived by the photometric method.

2. INSTRUMENTATION

The measurements of visible and infrared aurora contained in this report were obtained from optical instruments mounted in the Air Force Geophysics Laboratory NKC-135 aircraft. The aircraft provides an excellent platform for measuring aurora since it provides not only mobility but also the ability to fly above clouds and above the strong thermal infrared emission of the lower atmosphere.

The primary optical instrumentation consisted of a SWIR radiometer, a narrow field photometer, and a low light level television (LLLTV) viewing through the top of the aircraft 13° forward of the zenith. This configuration enabled the instruments to view approximately along the magnetic field lines when the aircraft was in the auroral zone flying magnetic south. The SWIR radiometer and narrow field photometer had essentially matched fields of view ($0.36^{\circ} \times 0.36^{\circ}$) which could be accurately aligned using an optical bench mounted onto the outer surface of the aircraft. The optical bench and alignment technique has been described by Sluder et al.⁵ The low light level television field was larger ($17.5^{\circ} \times 23^{\circ}$) and contained alignable fiducial marks to indicate the field of view of the radiometer and photometer. Secondary optical instruments consisted of a near infrared radiometer (NIR),⁷ for monitoring OH at $1.7 \mu\text{m}$, a 12-channel photometer, and an all sky camera.¹ Table 1 gives a summary of the instrumentation.

2.1 SWIR Radiometer

The SWIR radiometer is a vacuum jacketed, liquid nitrogen cooled radiometer with InSb detector and coated germanium and silicon refractive telescope. The radiation is modulated by a tuning fork chopper and filtered by a bandpass interference filter before reaching the detector. The telescope, chopper, filter wheel and detector are all conductively cooled by a liquid nitrogen reservoir within the vacuum jacket. The telescope views through a sapphire window and an optical baffle which are cooled and kept frost free by a continuous flow of cold nitrogen gas supplied by an auxiliary liquid nitrogen vaporizer. The window and optical baffle are exposed to the air outside the aircraft. Cooling the entire optical path reduces the background flux on the detector and significantly improves the sensitivity.

The relative spectral response of the radiometer, as measured by the AFGL/OPR Brower Labs monochromator, is shown in Figure 2. The absolute spectral responsivity was calibrated using both a bolt-on coolable extended source and an external warm Barnes 12-inch by 12-inch extended source. A cold neutral density filter was installed in the sensor during the warm extended source test and the monochromator test, which permitted the sensor to view the ambient environment without saturating.

7. Huppi, R.J. (1977) A versatile radiometer for infrared emission measurements of the atmosphere and targets, Opt. Eng. 16:485.

Table 1. Instrumentation Characteristics

INSTRUMENT	SPECTRAL RESPONSE			FOV	ZENITH ANGLE			APERTURE DIAMETER
	APR 79	SEP 79	AUG 80		APR 79	SEP 79	AUG 80	
SWIR Radiometer	2.85 - 3.152 μm		8 KR	0.28° FA 0.32° RL	13° FWD		InSb 77° K	5 cm
Narrow Field Photometer	3902 - 3914A 5556 - 5585A	3880 - 3907 5559 - 5584	0.4 KR at 50 KR 0.4 KR at 50 KR	0.36° FA 0.36° RL	13° FWD		PMT Bi-Alkali	7 cm
NIR Radiometer	1.67 - 1.75 μm		16 KR	10° Circular	2° AFT	13° FWD	PbS	5 cm
LLLTIV	3400 - 4750A 5577A 6300A OPEN (S-20)	3400 - 4750 5577A 7500A (Long Pass) OPEN (6-20)	2.5 KR	17.5° x 23° OR 165°	18° FWD 2° AFT		LSIT VIDICON S-20	
12-Channel Photometer	4278A 5577A 6300A Others		0.1 KR	2° Circular	2° AFT FLT 906-910 13° FWD FLT 911	13° FWD Except FLT 925 2° AFT	PMT COOLED S-20 -20° C	5 cm
All Sky Camera	3800 - 6800A EK 2475 FILM			165°	2° AFT		EK 2745 FILM	

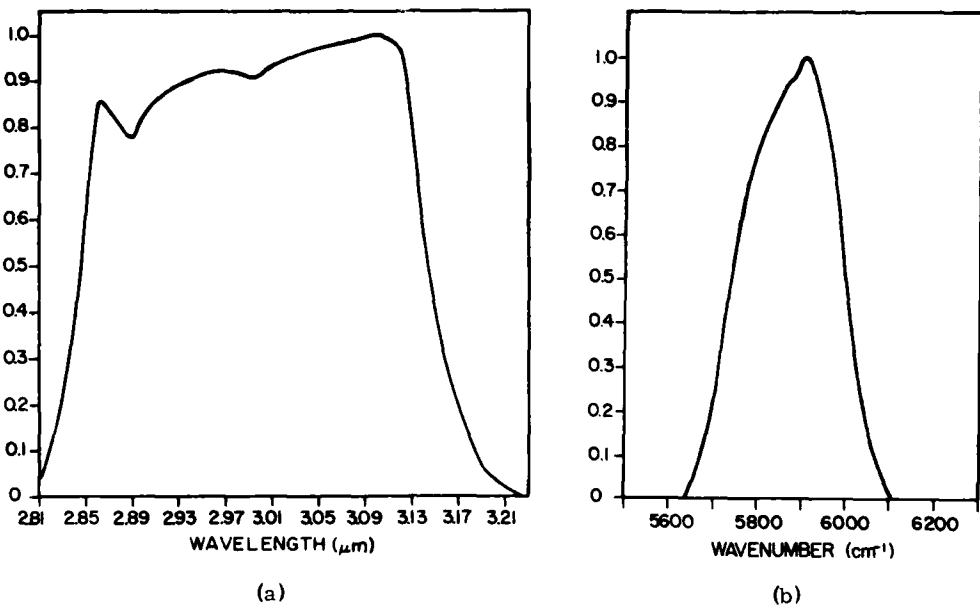


Figure 2. Spectral Response (a) SWIR Radiometer and (b) NIR Radiometer

2.2 Narrow Field Photometer

The narrow field photometer simultaneously measures 3914 \AA and 5577 \AA auroral emission over identical fields of view. This is accomplished by using a common telescope and field stop for both wavelengths. After the field stop the radiation is divided by a dichroic mirror. The short and long wavelength radiation is then filtered by separate interference filters before passing to separate photo-multipliers. A two-axis adjustment of the field stop permits alignment of the photometer field of view with the SWIR radiometer.

The spectral response of the photometer was determined by illuminating the full aperture of the photometer with collimated light from the Brower Labs monochromator. The spectral response for Flights 906-911 and 924-928 (1979), and Flights 023-029 (1980), is given in Figure 3. The spectral filters were changed in 1980 to provide a more nearly optimum spectral response. The absolute response for the 1980 flights was determined by viewing an extended diffuse reflective surface painted with Eastman White Reflectance Coating No. 6080 that was illuminated with both an NBS calibrated lamp (S/N:A299A) and a high temperature point source blackbody. Both techniques gave consistent results.

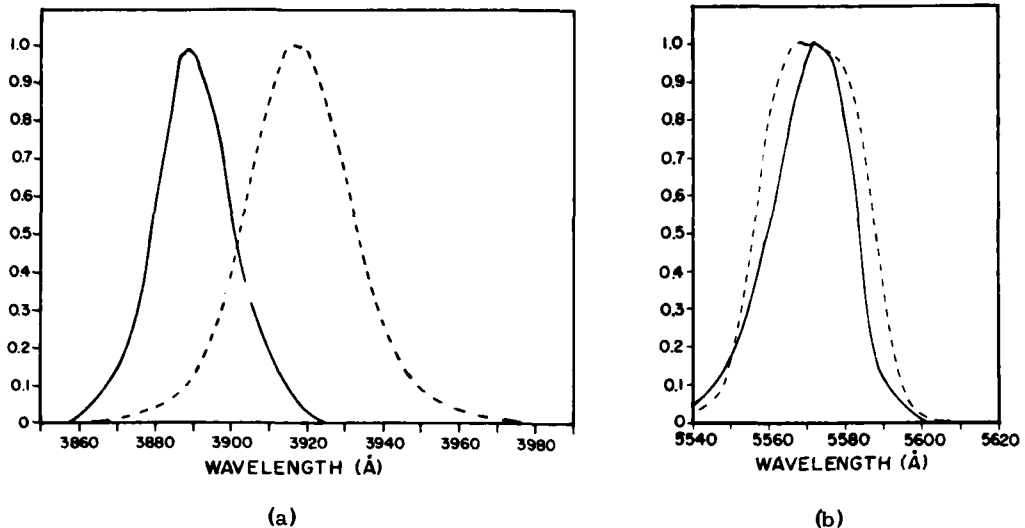


Figure 3. 3914\AA / 5577\AA Photometer Spectral Response (a) 3914\AA Channel, (b) 5577\AA Channel - Flights 906-911, 924-928, Solid Line; Flights 023-029, Dashed Line

Attempts to calibrate the narrow field photometer in the laboratory for the 1979 flights led to erroneous results. The initial measurement of the spectral response was found to be incorrect because the full entrance aperture was not illuminated; a spectral leak was found in the 3914\AA filter which made calibration with a blackbody source difficult; and results from a collimated blackbody source and an extended low brightness source did not agree. Because of this, absolute calibration of the photometer for the 1979 flights was determined by cross-correlating the photometer auroral measurements with simultaneous auroral measurements obtained with the 12-channel photometer which had several years of consistent calibration history.⁸

The responsivity of the SWIR radiometer, NIR radiometer and narrow field photometer are listed in Table 2 for all the 1979 and 1980 flights. The responsivity for the SWIR and NIR represents the values at the peak of the spectral response as shown in Figures 2 and 3 and have not been corrected for any spectral distribution. The NIR radiometer values are for a post amplifier gain of 1. The responsivity for the 5577\AA channel of the narrow field photometer is the

8. Kofsky, I. L., Villanucci, D. P., and Sluder, R. B. (1980) Evaluation of Infrared Simulation Data, Final Report for Contract DNA 001-80-C-0010.

Table 2. Instrument Responsivity

Flight No. Date	Narrow Field Photometer		SWIR Radiometer	NIR Radiometer (Ch 2)
	3914	5577		
906 and 907 21 Apr 79; 23 Apr 79	4.5×10^{-3} V/kR	7.32×10^{-3} V/kR	5.27×10^{-4} V/kR	4.35×10^{-5} V/kR
908 - 911 25 Apr 79; 1,2 May 79	2.94×10^{-2} V/kR	2.49×10^{-2} V/kR	1.76×10^{-4} V/kR	4.35×10^{-5} V/kR
924 - 928 17 Sep 79 - 28 Sep 79	6.9×10^{-3} V/kR	5.56×10^{-3} V/kR	1.76×10^{-4} V/kR	4.35×10^{-5} V/kR
023 7 Aug 80	3.77×10^{-3} V/kR*	1.2×10^{-2} V/kR	1.76×10^{-4} V/kR	3.76×10^{-5} V/kR
024 - 029	2.76×10^{-2} V/kR	1.2×10^{-2} V/kR	1.76×10^{-4} V/kR	3.76×10^{-5} V/kR

*This calibration is somewhat in doubt.

responsivity at 5577 Å. The responsivity for the 3914 Å channel is corrected for the integral of the radiation from the 3914 Å N₂⁺ band.

2.3 Low Light Level Television

The LLLTV consists of an ISIT television tube and selectable lenses which provide either a 17.5° by 23° field of view or a 165° diameter all-sky field of view. The spectral response is determined by one of four selectable filters in combination with the S-20 response of the ISIT tube. When the 17.5° by 23° lens system is used, an illuminated adjustable reticle is used to indicate the 0.36° by 0.36° portion of the field which is viewed by the photometer and radiometer. The spatial resolution with the 17.5° by 23° optics is about 0.12° by 0.12°. This system has been described in more detail by Sluder et al.⁹

3. DATA ANALYSIS

A total of 15 data segments from 10 flights representing about 70 min of high quality measurements were initially selected from the data base for analysis. The criteria used in choosing the samples were as follows:

9. Sluder, R. B., Andrus, W., Kofsky, I. L., and Villanucci, D. P. (PhotoMetrics, Inc.) Private communication.

- a. High signal to noise; generally IBC II+ aurora or greater
- b. Fractional illumination of aurora including totally sunlit, twilight and nighttime segments for investigation of SWIR yield dependence on solar angle
- c. Apparent delay (or lack of delay) of SWIR emission with respect to particle-energy input, during both day and night auroral measurements for comparison with solar angle.

Calibrated radiance traces from the SWIR radiometer and narrow field dual channel fluorescence photometer for each data segment are documented in Appendix A. Also included are traces from the wide-field NIR radiometer which monitors a region of the OH $\Delta v = 2$ overtone ($1.66 - 1.74 \mu\text{m}$) and whose optical axis pointed in the zenith in 1979 and was nominally coaligned with the prime instruments in 1980. Background airglow emission from the hydroxyl $\Delta v = 1$ sequence which overlaps the SWIR's bandpass can be scaled from the NIR readings and then subtracted from the $3 \mu\text{m}$ intensities. The ratio of in-band OH fundamental to overtone emission has been calculated to be about 2.5:1.

It should be noted that the narrow field photometer was a new design whose initial calibration is only indirectly applicable to the 1979 measurements (see Section 2). Final calibration (for 1979) was determined by cross-correlating the instrument's raw voltage readings with absolute intensities measured by the aircraft's 12-channel filter photometer (Reference 1) as described in Section 4 of Reference 8. No instrument performance irregularities were encountered in 1980.

3.1 Chemiluminous Yields and Delay Compared with Solar Illumination, Auroral Altitude and Magnetic Index

Table 3 lists several auroral and measurement parameters considered important in quantifying infrared visible correlations and assessing apparent chemiluminous yields. The entries in Table 3 are as follows: The first column lists the case number assigned to each data segment. Next is flight data and time of meridian passage (which is needed to determine solar elevation) at the midpoint of the data segment, whose duration is in the third column. Aircraft position, fuselage heading, and direction of the flight trajectory follows; the latter two azimuths typically differ by a few degrees because of crosswinds. When the fuselage is oriented at 180° magnetic, the coaligned input-and-output-measuring instruments point up the field lines.

The elevation angle of the center of the solar disk at the aircraft's zenith and (the directly applicable figure) at the latitude and longitude of the 120 km altitude intercept of the 13° forward fields follows the solar declination (also included because it is an input to the program for calculating solar elevation). Symbols D and I indicate decreasing (evening twilight) or increasing (morning twilight) elevation, to indicate whether the region had been sunlight "predosed." The next

Table 3. Auroral and Observation Parameters During SWIR Enhancements

CASE	FLIGHT #/DATE MERIDIAN PASSAGE	TIME (Z)	A/C POSITION Lat Long	TRAJECTORY Azimuth True Nadir Lat	SOLAR ALTITUDE (degrees)	SOLAR ANGLE (not 13 deg corrected)	HEIGHT (km) (h = 0.986 ²)	HATIG ⁺⁺		PLATE #(1173.6 ⁺⁺) PHOTON/PHOTON (km)	
								SOLAR ALTITUDE (13 deg corrected)	HATIG ⁺⁺ (6.30/0.278/15.37/39.16) photons/photon		
1	907/23 Apr '79 1158 TMP (250,23)	02:48 02:50:20	54°,69' 52,99' 65,35'	67°,16' 67,16' 65,35'	01.7 0.07 0.07	02.9 01.2 01.2	-21.30 -21.30 -21.30	433.0 455.1	6.5/16.5 6.5/16.5	119.5	
2	909/27 Apr '79 0240	02:37 01.36	71,30 71,76	321 321	360 360	331 331	-13.64 -13.64	-10.75 -10.75	113.3 109.9	111,1/14.9 84.8/3.2	
3	02:13 02:16	58,90 59,22	68,67 68,93	325 325	360 360	338 338	-13.6 -13.6	-12.14 D -12.02 D	138.0 136.2	7.9/18.3 7.7/3.1	
4	02:20	59,58 60,57	69,40 69,67	325 325	360 360	338 338	-13.6 -13.6	-11.89 D -11.89 D	136.8 136.8	9.6/24.3 9.6/76.6	
5	02:56 02:59	61,76 61,65	69,61 69,28	144 144	180° 180	155 155	-13.4 -13.4	-12.31 -12.38 D	148.5 160.6	5.1/6.4 5.1/8.6	
6	0908/25 Apr 1158	0837 0840	67,00 67,36	67,31 67,66	340 340	360 360	34+	-23.42 D -22.89 D	531.1 507.2	4.9/11.9 4.9/34.5	
7	924/18 Sep 1154	0016 0019	58,36 58,20	73,57 74,12	281 269	316 306	279 269	2.19 -9.40 D	82.6 85.5	11.9/10.9 73.8/31.6	
8	926/25 Sep 1152	0016 0022	58,04 57,32	77,67 78,02	265*	392*	-1.54	-11.05 D -10.84 D	96.7 117.3	6.4/8.2 6.5/173.6	
9	927/27 Sep 1151	0220	58,77 55,95	68,53 69,13	327 327	326 326	327 327	-1.35 -1.35	-30.70 D -30.47	909.9 905.7	2.5/1.3 13.7/5.6
10	928/29 Sep 1151	0119 0123	57,10 56,76	76,59 77,27	230 230	269 269	228 228	-2.11 -2.11	-20.13 -20.53 D	397.1 204.8	4.5/11.87 4.4/12.45
11	023/07 Aug '80 1206	0654 0704	62,99 63,34	112,02 [*] 124,75	284 284	252 252	16,36 16,36	-9.12 D -8.75 D	79.2 -8.62	2.6/9.0 72.8	
12	026/18 Aug 1236	1125 1126	63,06 63,16	157,49 [*] 147,36	02.9 02.9	360 360	330 330	-10.10 I -9.95 I	106.0 97.0	6.1/19.6 6.1/19.6	
13	1159 1203	64,36 63,93	148,43 [*] 148,95	21.9 21.9	177 177	207 207	-9.31 I -9.61 I	86.9 90.5	4.4/12.45 3.9/12.45		
14	027/19 Aug 1204	1924 1030	64,30 64,93	148,42 [*] 147,65	02.6 02.6	358 358	12.65 12.65	-12.89 I -12.13 I	162.8 146.7	11.8/1.2 11.8/1.2	
15	1055 1109	65,05 61,98	147,46 [*] 149,12	21.2 21.2	179 179	208 209	-11.45 I -12.36 I	128.5 145.2	4.7/1.1 4.7/1.1		

* After flight 023, refers to latitude/longitude of intercept at 120 km of the 13°-tilted instruments.

** 12-channel photometer readings at maximum auroral column brightness, to zenith in flights 909, 918 and 927.

Bracketed values are from narrow-field photometer

++ K's refer to College, AK section

* Aircraft is turning to S 0915:38 - 0917:56

column is the hard earth's shadow height with no correction for atmospheric refraction (see Figure 27 of Reference 4). The earth's shadow height is not an accurate altitude for ultraviolet illumination because solar radiation is scattered and absorbed as it passes tangentially through the earth's atmosphere. The tangent altitude at which 1/2 the incident solar flux is transmitted through the (1966 U.S. Standard) atmosphere is 34 km at wavelength 3400Å, 45 km at 3050Å, and 70 km at 2380Å. To a good approximation, the minimum auroral altitude reached by half these ultraviolet photons can be found by adding "screening" heights to the illuminated height listed in Table 3.

Column intensity ratios of optical-auroral emission features at the time in the data segment when the energy input rate is a maximum are listed next. The altitude of peak energy deposition at this time, calculated from the 6300Å/4278Å ratio and 4278Å intensity follows. In Flights 908 and 909, before the wavelength-cycling photometer's field had been directed 13° forward, these altitudes refer to the aircraft zenith; in other flights they refer to the excitation in the fields of the coaligned 0.36° instruments.

The last two columns list the three-hour local (K) and global (K_p) magnetic indexes. Local K 's refer to the College, Alaska sector and thus are not directly applicable to the 1979 flight series (conducted from Pease AFB, N.H.).

The data set in Table 3 includes measurements on both stable arcs and less structured (diffuse) aurora that were illuminated to varying degrees, with direct (and scattered) solar radiation. Fractional illumination of the emitting region for each case (Table 4) was determined by first assigning a model energy deposition altitude profile to each arc (or glow) based on the peak altitudes in Table 3 and following the procedure in Reference 10. The altitude distribution of incoming particle flux was assumed to remain fixed for the 2-3 min duration of the measurement interval. (For Cases 15a and b, an average peak altitude somewhat higher than that listed in Table 3 was used in the calculation.) An estimate was then made for the fractional energy deposition rate lying above the hard earth illuminated height defined in column 10 of Table 3.

Table 4 shows that a sampling of day, night and twilight measurements are included in the selected data. Six cases were identified as being totally sunlit (three each from the 1979 and 1980 series). A further six cases represent partially illuminated auroras (again, three cases from each flight series), while the remaining three are nighttime. It should be remembered that the entries in Table 4 do not reliably reflect the increased outscattering of UV photons at lower tangent heights. That is, a recalculation of Table 4's fractions for 2500-3500Å radiation would have the effect of decreasing the fractional illumination values.

10. Rees, M.H., and Luckey, D. (1974) Auroral electron energy derived from ratio of spectroscopic emissions, J. Geophys. Res. 79:5181.

Table 4. Fractional Illumination of Aurora for the 15 Data Segments Identified by Case Number. Values refer to the "Hard Earth" definition of solar illuminated height as defined in the text

Percent Sunlit - Hard Earth Definition	
Case Number	Percent Sunlit
1	0
6	0
9	0
4	65
15a	68
15b	45
3	53
14	15
5	47
11	100
7	100
13	100
12	100
8	100
2	100

To quantify spatial and temporal correlation between particle energy input and infrared output, and to evaluate absolute SWIR yields, cross-plots of the simultaneously measured 3914A and 3 μm band radiances were made. First, the data traces were manually smoothed, then intensities were read at nominally 5 sec intervals. For cases where the duration of enhancement was short (case 12 for example), the sampling interval was reduced to approximately 1/2 to 1 sec.

Emission from the hydroxyl $\Delta v = 1$ sequence which overlaps the SWIR radiometer bandpass was usually not subtracted from the 3 μm readings before plotting. As the contribution from this airglow remains essentially constant during individual

data segments, slopes of the cross-plots (which are a measure of the chemiluminous yield) are not expected to be distorted (or changed) by this baseline offset.

The projection of the instrument fields at altitudes where incoming particle energy is absorbed is traversed by the aircraft in about 4 sec, and the data smoothing, as mentioned above, is of the order of a few seconds. If these times are comparable to (or longer than) the time for aerochemical reactions to excite SWIR radiation, or if production and loss rates have reached equilibrium, the cross-plot method is a valid means for determining average chemiluminous yields.

Examples of results from three data segments representing day (Case 12), night (Case 1), and twilight (Case 3) measurements on the IBC+ aurora are shown in Figure 4. Column brightnesses refer to 1 sec intervals (Cases 1 and 3) on the radiance traces which had been previously filtered (each point on the original trace being an average of 11 points spaced 0.01 sec apart). For Case 12, the sampling interval was 0.4 sec.

The all-sky images in the appendix (nominal 4 1/2 sec exposures) show that the visible auroral distribution can best be described as a near-uniform arc for Cases 3 and 12, while Case 1 is a non-stationary "breakup". All of the photographs were printed with the same exposure to qualitatively indicate relative brightnesses.

Some of the SWIR enhancements (Case 12 for example) show obviously longer decay times or peak offsets when compared to the 3914Å fluorescence signal as is evidenced by the loop formed by the points in Figure 4c. This effect is seen in both the twilight and nighttime flights and thus does not appear to be directly correlated with solar angle. (This point is discussed further below.)

The straight lines in Figure 4 are least-squares fits to the data points (the R values representing statistical correlation coefficients, or "goodness of fit" with a straight line). It has been assumed that the 3914Å band fluorescent intensities have negligible uncertainty in comparison with the 3 μ m band SWIR intensities, and that a linear relationship exists between the two variables. The assumed linearity is obviated by the curvature of points in Figure 4c as the fall time of SWIR radiance is longer (by about 5 seconds) than that for 3914Å fluorescence. However, the seven circled points in Figure 4c, which refer to the first 2 1/2 seconds of the 8 second measurement interval, show a high linear correlation when considered separately.

Slopes of the "best fit" lines can be interpreted as being proportional to the chemiluminous energy efficiency (or yield) for the nitric oxide overtone sequence if it is assumed that all of the SWIR emission is produced by vibrationally excited NO populated by $N(^2D) + O_2$ reactions (Section 1 of Reference 3). In Figure 4c the fit to all data points is a reasonable estimate to the average NO yield over the measurement interval as about an equal number of points lie above and below the line. [This assumption is further supported by a calculation ratioing the "area"

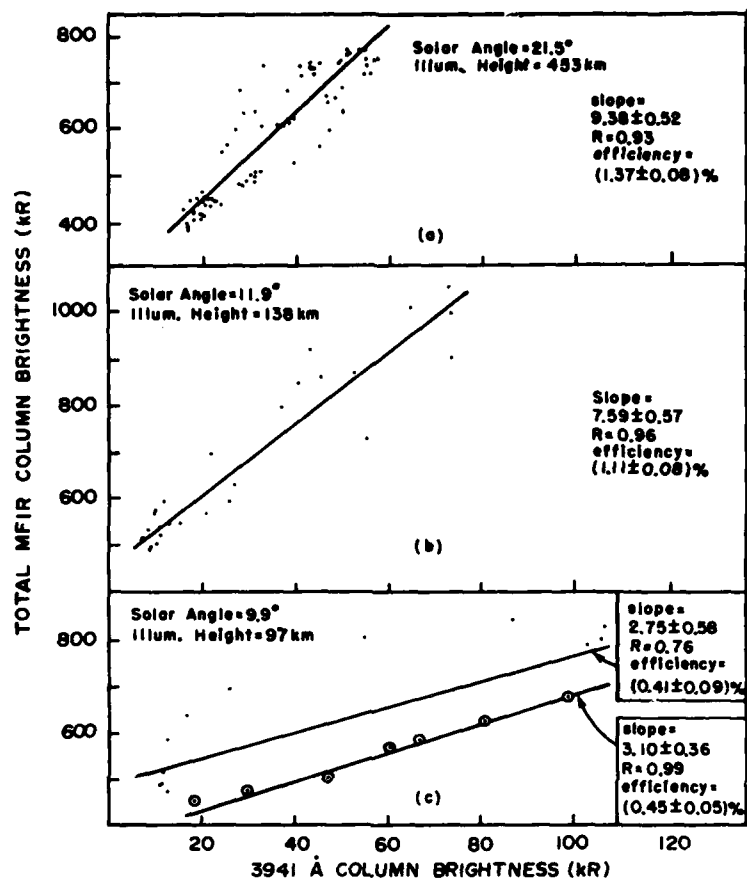


Figure 4. Cross-plots of $2.8-3 \mu\text{m}$ and 3914\AA Intensities Measured by the Narrow-field Instruments at Three Different Solar Depression Angles Representing (a) 0 Percent (Case 1), (b) 53 Percent (Case 3), and (c) 100 Percent (Case 12) Fractional Illumination. The straight lines are uniformly-weighted least-squares-fits. Confidence limits refer to 90 percent statistical certainty of the slopes; R-values are correlation coefficients as defined in Reference 2

(in $\text{kR}\cdot\text{sec}$) under the SWIR enhancement to that under the 3914\AA peak which shows the average "integrated" photon ratio to be in agreement (within the limits of the calculation) with the best fit slope.) The uncertainties shown on Figure 4 refer only to 90 percent statistical confidence limits on the calculated slopes and thus do not reflect other sources of error such as instrument effects, window frost, etc.

Following the procedure in Reference 3, and taking 0.42 as the fraction of the NO $\Delta v = 2$ (COCHISE production model) sequence overlying the radiometer bandpass,

we determined chemiluminous yields from the cross-plots for each of the 15 segments (cases in which the aforementioned "area" method was used are identified). Results, listed in order of increasing solar depression angle, are shown in Table 5. The column labeled PhM delay is a semi-quantitative measure of the time that SWIR output "lags" energy input. The values were determined by visually comparing peak offsets and apparent decay time shifts between 3 μ m band and 3914A band data traces. A more rigorous, mathematical description of this temporal correlation using Fourier transforms is described in another section, results of which are summarized under the heading "MB LAG". Data quality (based on signal/noise of the data streams) follow; the times in the parentheses refer to duration of the enhancement interval. Fuselage pointing direction and altitude of peak energy deposition, adapted from Table 3, are in the last two columns. The average shown at the far right refers to peak emission altitude averaged over the observation interval.

The efficiencies listed in Table 5 show a statistically significant variability of about a factor of 2 over both the (long term) 18-month measurement period as well as among separate flights of each series (short term), and even within individual flights (for example, Cases 14 and 15 a and b, Flight 027). A similar variation was noted in the data obtained by the wide-field instruments in 1975-1978 (Reference 3) where the average efficiency was found to be about 1/2 percent. Here, the mean yield appears closer to 1 percent, and in some cases as high as 1.4 percent.

To verify, or at least identify, probable sources of this variability, cross-correlation plots relating several of the likely auroral and measurement parameters to the average overtone yield were made (Figures 5 and 6). The circled numbers refer to the specific case numbers in Tables 1 and 5. Figure 5a shows no apparent correlation with absolute 3914Å band level which is not unexpected as most of the individual cross-plots of 3 μ m band versus 3914A band radiances are generally linear. Results from the earlier wide-field measurements support this finding (Reference 3).

Figure 5b and d also indicate that SWIR efficiency is independent of fractional auroral illumination and global magnetic index. Further, no correlation was found between efficiency and aircraft altitude (not shown). Some evidence for a dependence on the ratio of hydroxyl fundamental to overtone emission is in Figure 5c, however, the apparent trend [negative slope; (-3.2 \pm 2.2) of the ratio $\Delta v = 1$ photons per $\Delta v = 2$ photons plotted against percent change in yield] is opposite to what one might reasonably expect. That is, if the OH ratio had been artificially increased (due to the presence of cirrus clouds in the instrument field of view, for example) the result would probably be higher efficiencies (positive slope) due to increased outscattering of shorter wavelength photons. It is not clear whether frost on any of the viewing windows could produce the effects seen in Figure 5c. In any case,

Table 5. Chemiluminous Yields and Apparent SWIR Delays Derived From the 15 Data Segments Listed in Order of Increasing Solar Depression Angle and Compared with Peak Auroral Altitude and Aircraft Heading

Case	Solar Dep Angle (deg)	Ave. Eff. (percent)	MB Eff. (per- cent)	Delay (sec)	MB Lag (sec)	Data Quality -S/ N-	Fuselage Pointing Direction	Auroral Alt.(km) Peak:Ave*
11	8.8	1.36 ± 0.13	2.66	0	0.2	Fair-Good (350 sec)	W(Ferry)	116
7	9.3	0.70 ± 0.09	0.68	2-3	1.0	Good (180)	NW	160
13	9.5	0.92 ± 0.13 (0.8 "area")	1.04	5	1.0	Good (120)	S	119 124 +/-2
12	10.0	0.57 ± 0.10 ("area")		5	1.0	Good (8)	N	109
8	10.4	1.04 ± 0.10	0.75	0-1	1.0	Fair-Good (240)	S	130 144 +/-3
2	10.7	1.09 ± 0.30 ("area")	1.03	1.5-3	0.83	Very Good (150)	N	134
4	11.6	1.36 ± 0.17	1.22	2-6?	0.91	Good (210)	N	120
15	11.5	1st half 1.1±0.04	0.66	3	0.91	Good (300)	S	120 130 +/-5
	12.3	2nd half 1.2±0.40	1.37	2?	0.83	Good (240)	S	122 127 +/-2
3	11.9	1.11 ± 0.08	1.09	1-2	0.83	Good (45)	N	120
14	12.5	0.51 ± 0.08	0.93	1-2	0.91	Good (300)	N	11 122 +/-2
5	12.6	1.09 ± 0.08	1.03	3-4	0.83	Fair-Good (120)	S	128 137
1	21.5	1.37 ± 0.08	1.16	2-4	1.0	Good (140)	NE	120
6	23.0	0.80 ± 0.07	0.55	0-1	0.5	Good (180)	N	120
9	30.4	1.30 ± 0.21	1.31	0-1	1.0	Good (80)	N	145

*Altitudes are averaged over entire data segment.

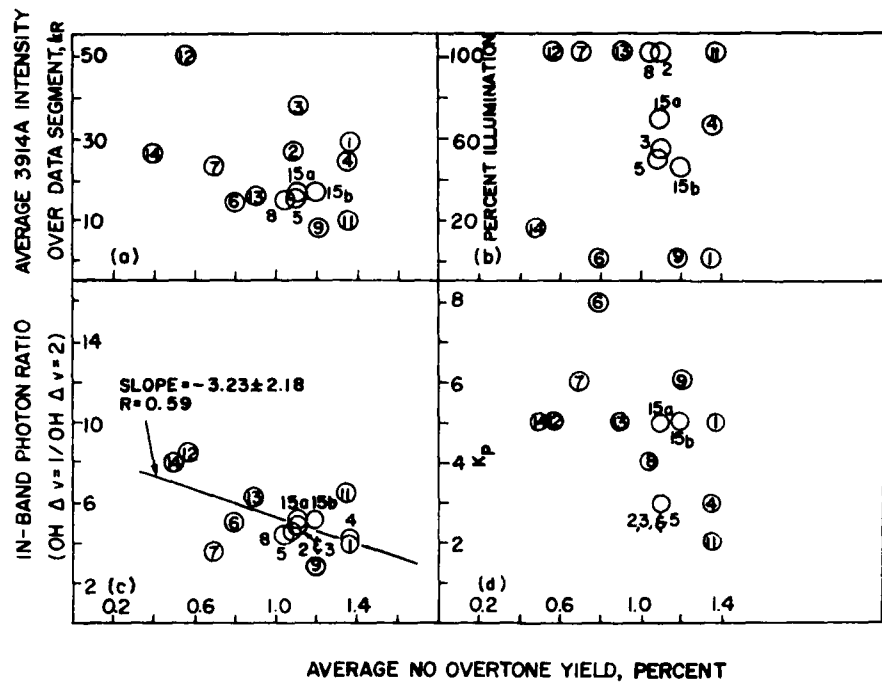


Figure 5. Average NO Overtone Yield Compared with (a) Average 3914Å Intensity, (b) Fractional Auroral Illumination, (c) Hydroxyl Fundamental/Overtone Ratio, and (d) Global Magnetic Index for the 15 Data Segments in Table 3

there are too few data points in Figure 5 to make a statistically compelling argument supporting the apparent anticorrelation. Additionally, the trend line is significantly "weighted" by the two data points from Cases 12 and 14 which further reduces the confidence that can be placed in the best fit slope.

Figure 6 shows that there is a weak correlation between average yield and the altitudes at which most of the incoming electrons deposit their energy. The altitudes on the bottom half of the figure are from Table 3 and thus refer only to that part of each data segment where the 3914Å column brightness was a maximum. For the five cases in which the aircraft was heading magnetic South, peak energy deposition altitudes were averaged over the duration of the measurement interval and are shown at the top of Figure 6.

The slope of the regression line fit to all data points is 3.6 (or an increase in efficiency of about 0.28 percent/km) and has a correlation coefficient R , of only 0.08, indicating a poor linear fit. If Case 7 is omitted, the slope becomes 16.8 (0.06 percent/km), $R = 0.49$, and the points lie reasonably close to the line. In

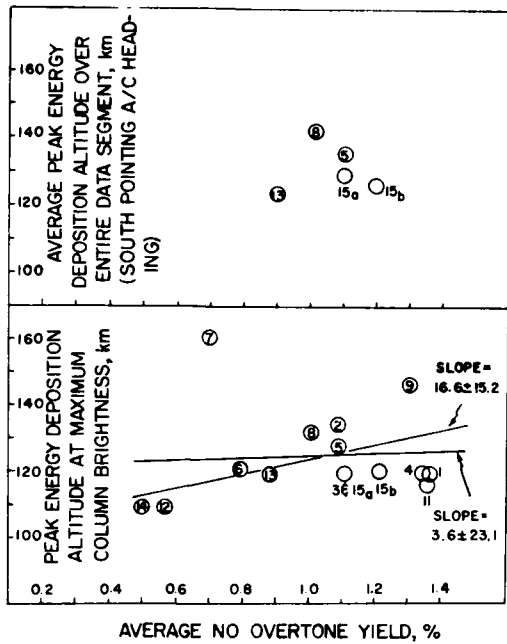


Figure 6. Average NO Overtone Yield for the 15 Data Segments Compared with Altitude of Peak Energy Deposition

both cases, the large uncertainty (90 percent statistical confidence limits) indicates that the slope of the best fit line could be as high as 32 (0.03 percent/km).

To further investigate this matter, "instantaneous" values for efficiency and altitude were determined at 5-sec intervals for Case 13 during which a uniform (sunlit) arc was scanned by the instruments. The results, which generally support Figure 6, suggest an increase in mean overtone yield of about 0.15 percent/km with an uncertainty of +0.18 percent, -0.05 percent/km. This finding, however, is in disagreement with the simple calculation shown on Figure 7 which indicates that the column integrated yields should be relatively insensitive to energy deposition altitude.

As previously mentioned, some of the SWIR enhancements have longer rise-and fall-times (up to 5 seconds) than the corresponding 3914 Å traces while others show no apparent lag. Determination of the delay times from Table 5 by visual inspection of data traces is a somewhat subjective evaluation procedure which depends in part on the time resolution of the data plots. As some of the original radiance traces were presented with more compressed time scales, less certainty

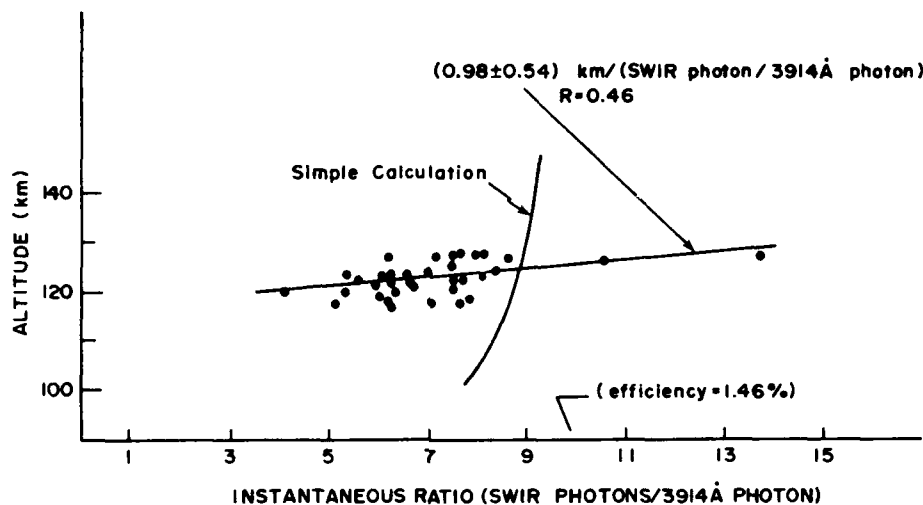


Figure 7. Instantaneous Ratio (SWIR/3914 \AA Photon) Plotted Against Instantaneous Peak Energy Deposition Altitude for Flight 026 (Case 13, 1159:30 – 1202:53), and Compared with Simple Calculation of Expected Altitude Dependence

can be placed on the delay times assigned to those segments. However, since some measurable offset of SWIR radiance is evident in almost all 15 cases, it is unlikely that this effect is an artifact of the data presentation. The Fourier transform technique indicates somewhat shorter absolute lags with a variability of a factor of 2.

In Table 6, the offsets are separated into two classes representing both short (≤ 2 sec) and long (> 2 sec) delays for comparison with various auroral and measurement parameters. The tabulated values refer to the number of data segments falling into each category. It is apparent that there is no statistically significant "favoring" of long or short delays under any heading as about an equal number of cases are included in each category.

Of particular importance is the lack of correlation with sun angle (or more importantly) fractional illumination of aurora. The cross-plot in Figure 8a, which identifies the delays by the case number, further quantifies this finding. (Included on the figure are some of the results from the Fourier treatment of the data.)

These data can be summarized as follows:

Table 6. Correlation of SWIR Enhancement Delay with Several Auroral and Measurement Parameters

Sun Angle	PhM Delay	
	≤2 sec	>2 sec
I < 10°	1	3
II 10° to 12°	2	3
III 12° to 14°	1	1
IV > 14°	2	1
I + II	3	6
III + IV	3	2
I + II + III	4	7
IV	2	1
Pointing: N	1	3
S	4	5
Efficiency: > 1 percent	5	5
≤ 1 percent	2	3
Height: < 120 km	2	2
120 km	2	3
> 120 km	2	3
Form: Isolated Arc (IA)	4	4
Other (O)	2	4
IA North Heading	3	2
IA South	1	1
O North	1	3
O South	0	2
Spring 79	2	4
Fall 79	2	1
Fall 80	2	3
OH Level: < = 300 kR	5	3
Δv = 1 > 300 kR	2	5
K _p : 1 - 4	3	3
5 - 8	4	5

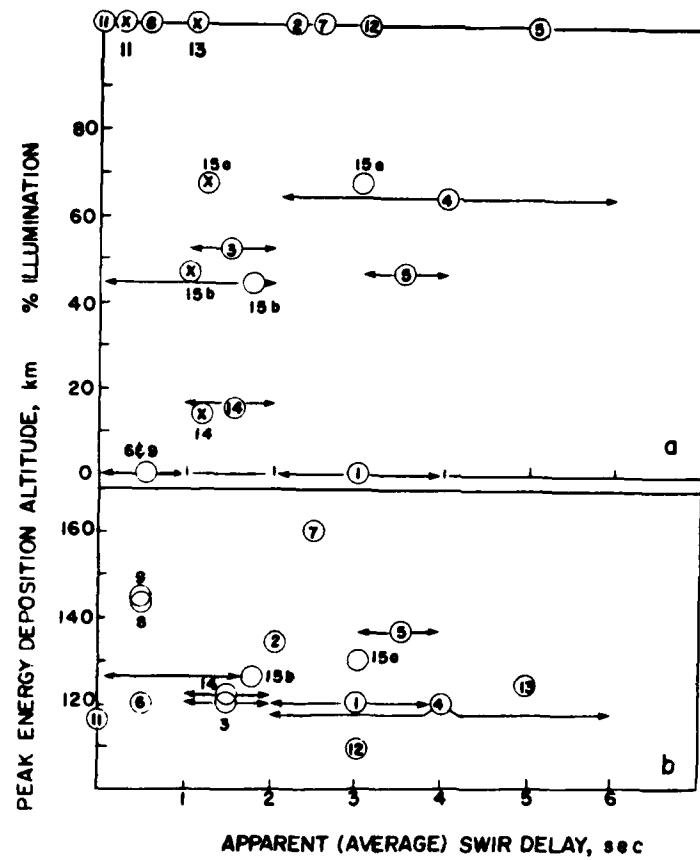


Figure 8. Apparent SWIR Delay Compared with (a) Fractional Auroral Illumination and (b) Peak Energy Deposition Altitude for the 15 Data Segments. Points marked \otimes are from the Fourier treatment of the data

- Cases 100 Percent Sunlit 6
- Cases < 100 Percent, > 0 Percent Sunlit 6
(Range 0.15 to 0.68 Sunlit)
- Cases 0 Percent Sunlit 3

Note: "Sunlit" refers to hard earth definition -
Altitude in km = 0.98 (SDA in degrees)²

Percent Sunlit	PhM Delay	
	≤ 2 sec	> 2 sec
100 Percent	2	4
< 100 Percent, > 0 Percent	3	3
0 Percent	2	1

Figure 8b shows the dependence of average SWIR delay on peak energy deposition altitude. Again, no correlation between the two variables is evident.

It should be noted that some of the 5577Å enhancements also appear to lag the energy-input monitoring 3914Å channel (Cases 1 and 3, for example). However, in all cases, the offsets are found to be < 2 seconds when the same method of visual inspection is applied to the data.

3.2 3 μ m and 5577Å Time Response and Efficiency Using Fourier Transform Technique

The delay of 5577Å emission and 3 μ m emission relative to the prompt 3914Å emission has been determined by visually inspecting intensity versus time plots of the sampled and plotted data of the three channels. A more quantitative method of determining the delay, which involves the frequency analysis of the three signals, is presented here along with a speculative chemistry model which is in general agreement with frequency analysis of the measured data.

Short time segments consisting of 2048 data points that include the passage of the photometer field of view across auroral features are digitized. The broad band analog filtering of the three data channels was carefully matched before the samples were taken so that no artificial relative delay was introduced. This discrete set is then numerically processed by a Fast Fourier Transform program on a Digital PDP-8E computer to give frequency transform spectra of 1024 complex points. This is done for all three channels, the 5577Å, 3914Å, and 3 μ m pulses for a common starting time. We then ratio the transforms in the frequency domain to determine the transfer functions, assuming the 3914Å pulse reflects the time dependency input to a linear chemistry system. The measured transfer functions are then filtered and fit to either a theoretical single or double pole function by selecting quenching coefficients which give the best fit. In general, we are able to derive a simple pole from most pulses, which shows a surprisingly similar value around 1.2 sec^{-1} from pulse to pulse, for the 5577Å/3914Å transfer function as well as the 3 μ m/3914Å transfer function.

Figure 9 shows a sample of infrared 3 μ m data measured on Flight 909 and referred to in this report as Case 3. This sample of data has a duration of 102.40 seconds starting at 2 h 13 min 57 sec. Figure 9 also shows the imaginary and real components of the Fourier transform of the data sample. The radian frequency is proportional to the Kth transform point and is given by

$$\omega = 2\pi K / (\text{sample duration in sec})$$

In Figure 9, the maximum point plotted is K = 64 which corresponds to a frequency of 3.93 radians per second. Figures 10 and 11 are the data samples and Fourier transforms for the 3914Å and 5577Å channels.

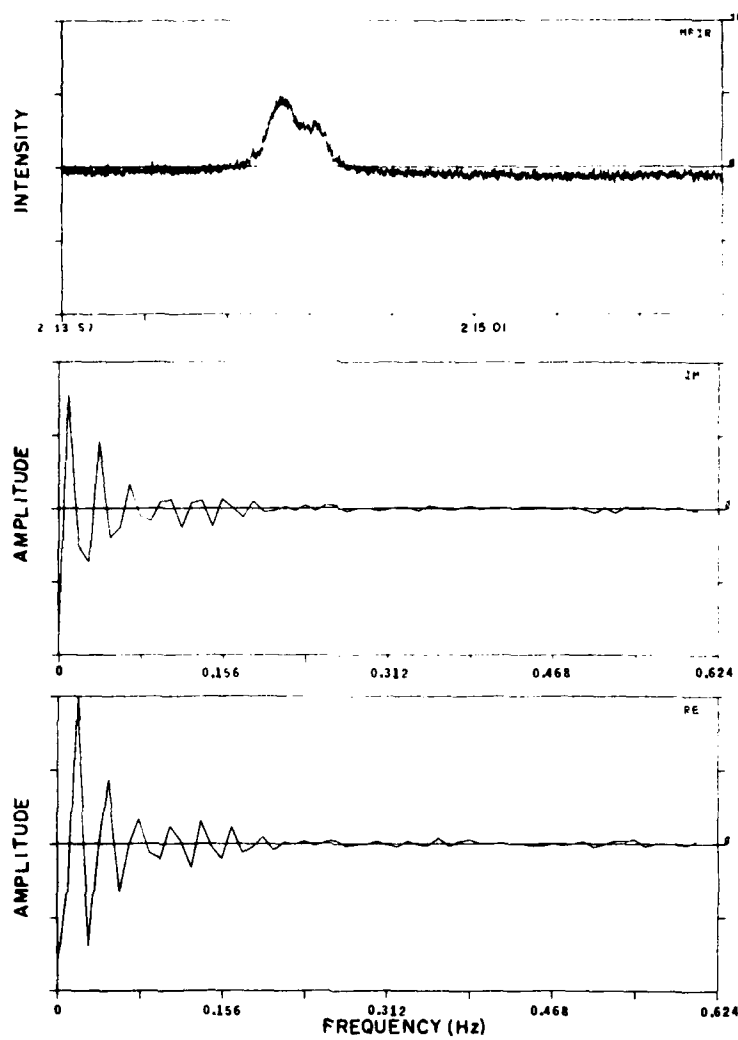


Figure 9. (Upper plot) $3\mu\text{m}$ Auroral Emission Measured 2:13:57 GMT, 27 April 1979, Flight 909, Case 3. (Center plot) Imaginary component of Fourier transform. (Lower plot) Real component of Fourier transform. Time scale: 12.8 sec/division, frequency scale: 0.078 Hz/division

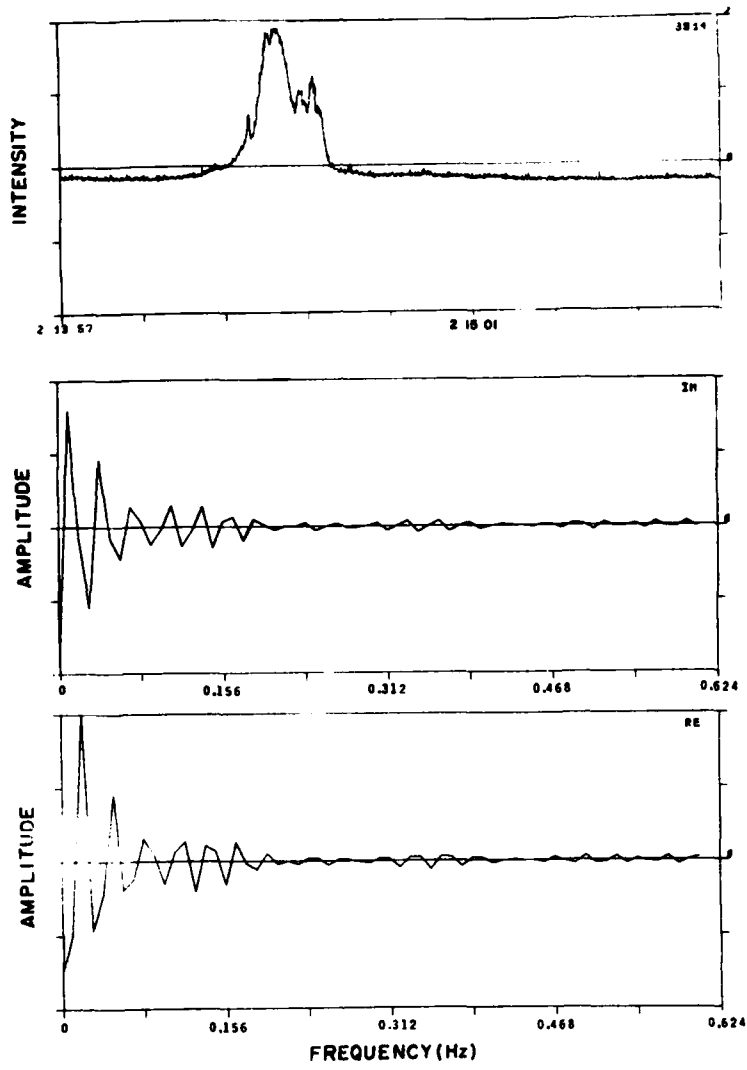


Figure 10. 3914Å Signal and Corresponding Complex Fourier Transform of Data Measured 2:13:57 GMT, 27 April 1979, Flight 909, Case 3

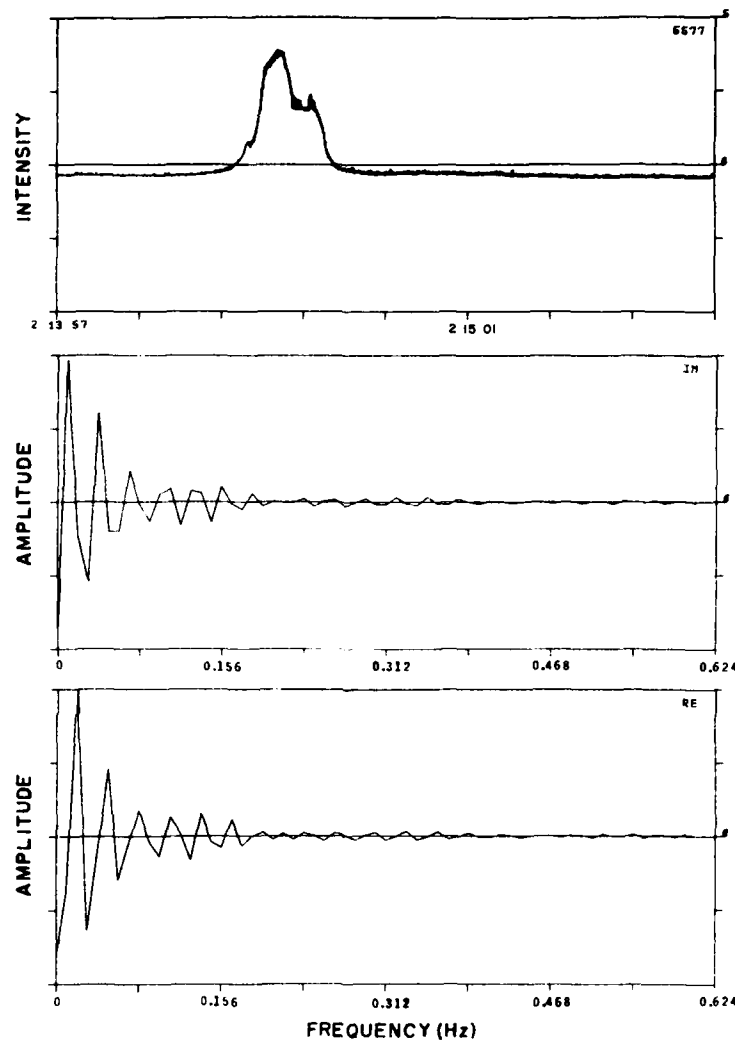


Figure 11. 5577 \AA Signal and Corresponding Complex Fourier Transform of Data Measured 2:13:57 GMT, 27 April 1979, Flight 909, Case 3

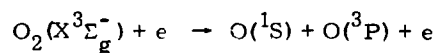
The ratio of the transforms of the 3 μm divided by the 3914 \AA is the transfer function and is shown in Figure 12. The upper two plots are shown before filtering and the lower plots are the same data after filtering. The filtering consists of a Fourier transform-filter-inverse-Fourier transform technique designed to pass only the lower frequencies, because much of the noise is more shot-like than Gaussian. Figure 13 shows the corresponding unfiltered and filtered transfer function for the 5577 \AA /3914 \AA radiation.

The filtered complex transfer function was used to determine the best-fit quenching coefficients and photon ratio of 3 $\mu\text{m}/3914\text{\AA}$ and 5577 $\text{\AA}/3914\text{\AA}$. The 15 cases were analyzed with this technique and the results are summarized in Table 7. Results for all 15 cases are given by Bruce and Eastman.¹¹ The delay of the 3 μm or 5577 \AA signals relative to the 3914 \AA is the inverse of the quenching coefficients and is typically on the order of 0.8 sec. The delays, as determined by the Fourier analysis, are listed in Table 5 in the column labeled MB Lag and are seen not to be in consistent agreement with delays obtained by visual inspection of the data plots.

The 3 $\mu\text{m}/3914\text{\AA}$ photon ratios listed in Table 7 assume that all the emission occurs at the peak of the spectral response of the radiometer. If the emission is assumed to be from NO and the atmospheric transmission and the spectral response of the radiometer are taken into account, then the efficiency can be calculated by multiplying the 3 $\mu\text{m}/3914\text{\AA}$ photon ratios in Table 7 by 0.146. These efficiencies are listed in Table 5 under MB EFF. The efficiencies obtained from the Fourier analysis agree, in most cases, with those obtained from the cross-plot method but disagree as much as a factor of 2 in some cases.

3.2.1 THE O(¹S) PULSE PRODUCTION

A number of chemical reactions leading to O(¹S) production have been proposed. They include direct processes such as the electron impact dissociation of molecular oxygen,



and the electron impact excitation of atomic oxygen,



For the atmospheric region considered here these are considered to be of minor importance.

11. Bruce, M., and Eastman, C. (1981) Frequency Analysis of Visible and Infrared Auroras, Utah State University Report No. EDL-SRL-81-4.

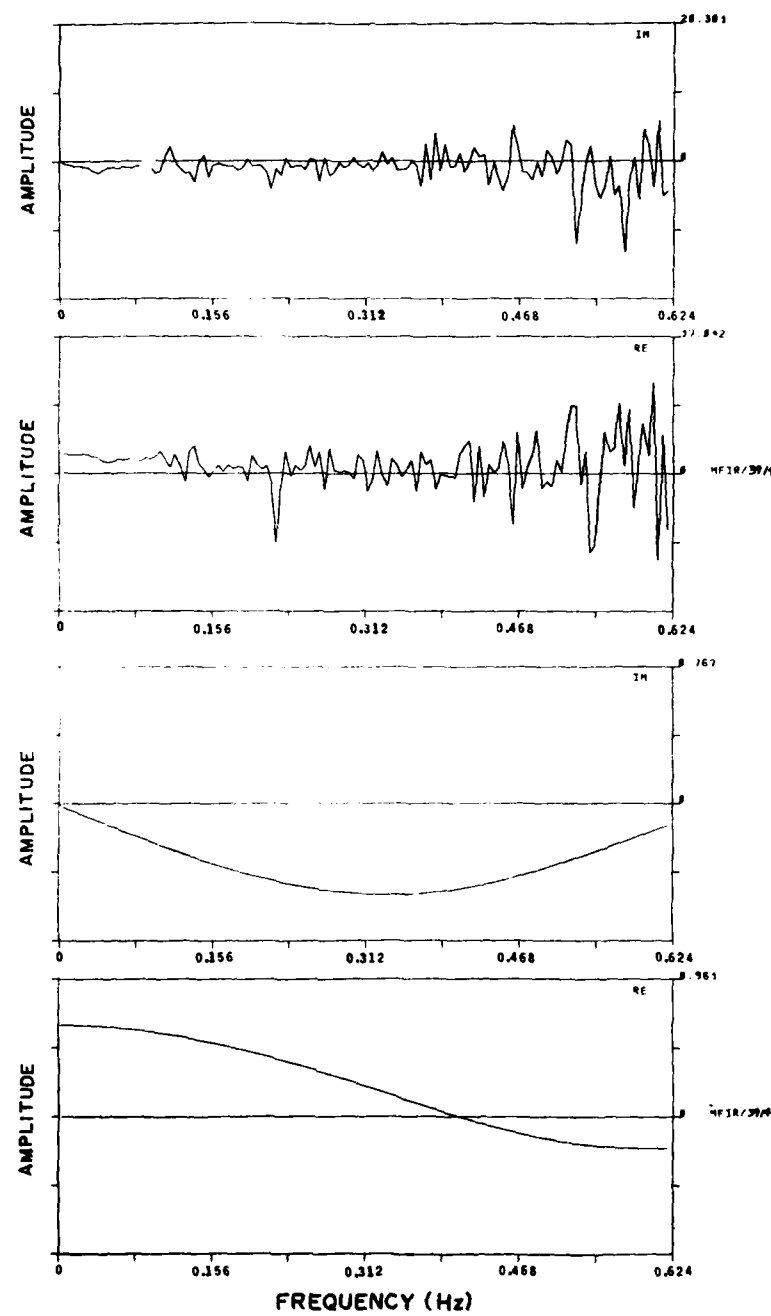


Figure 12. Complex Transfer Function (Unfiltered, Upper; Filtered, Lower) of 3 μ m Response on 27 April 1979. Data sample measured 2:13:57 GMT, Flight 909, Case 3. Frequency scale: 0.156 Hz/division, 0.98 radians/division

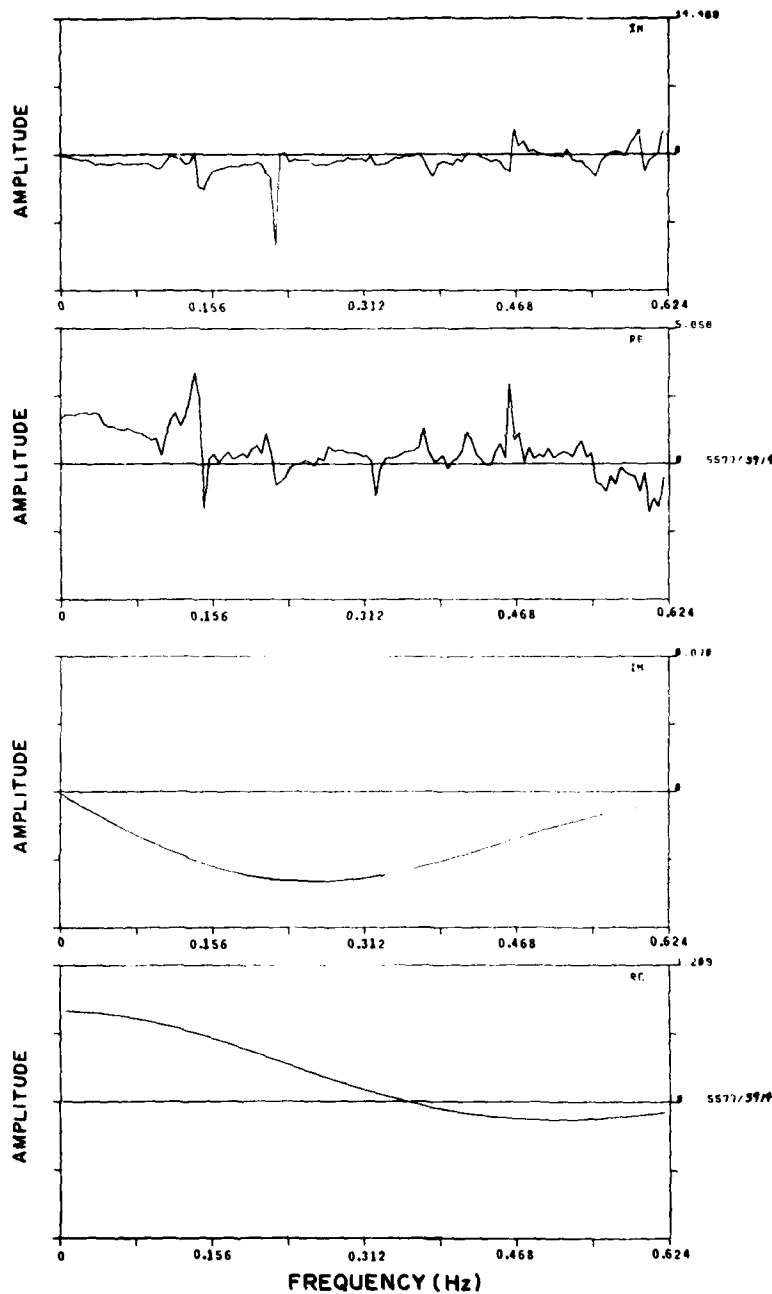


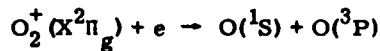
Figure 13. Complex Transfer Function (Unfiltered, Upper; Filtered, Lower) of 5577 Å Response on 27 April 1979. Data sample measured 2:13:57 GMT, Flight 909, Case 3. Frequency scale: 0.156 Hz/division, 0.98 radians/division

Table 7. Photon Ratios and Quenching Coefficients

Case #	Flight	Time	Sample Duration (sec.)	Quenching Coefficient $\left[\frac{3.5\mu\text{m}}{3914} \right] (\text{sec.}^{-1})$	Photon Ratio (Average) $\left[\frac{3.5\mu\text{m}}{3914} \right]$	σ^2 Variance	95% Confidence Interval \pm	Quenching Coefficient (sec.^{-1})	Photon Ratio $\left[\frac{3.5\mu\text{m}}{3914} \right]$	σ^2 Variance	95% Confidence Interval \pm	Photon Ratio $\left[\frac{3.5\mu\text{m}}{3914} \right]$
13	026	12:00	184.32	1.0	7.14	3.37	1.27	1.2	2.00	0.0424	0.134	0.281
11	023*	06:55	368.64	1.2	18.20	116.10	7.04	1.5	2.89	0.132	0.225	0.159
14	027	10:24	368.64	1.1	6.35	7.38	1.68	1.5	2.26	0.0205	0.0887	0.356
15	027	10:55	368.64	1.1	4.51	8.91	1.75	1.2	1.67	0.720	0.527	0.370
15	027	11:01	368.64	1.2	9.38	61.50	4.86	1.2	2.33	0.112	0.225	0.248
6	908	06:37	184.32	2.0	3.76	4.07	1.25	2.0	1.99	0.0177	0.0824	0.529
2	909	02:37	184.32	1.2	7.06	3.29	1.12	1.2	1.99	0.475	0.450	0.282
5	909	02:56	184.32	1.2	7.04	18.50	2.67	1.2	1.78	0.1750	0.170	0.253
4	909	02:18	368.64	1.1	8.33	50.50	4.41	1.2	2.35	0.508	0.442	0.282
3	909	02:14	102.40	1.2	7.49	1.13	0.660	1.2	2.47	0.0326	0.112	0.330
1	907	02:48	184.32	1.0	7.93	5.95	1.81	1.2	2.46	0.119	0.214	0.310
7	924	00:16	184.32	1.9	4.66	1.41	0.735	1.1	2.65	0.121	0.215	0.569
8	926	00:16	368.64	1.0	5.16	7.45	1.69	1.0	2.39	0.833	0.633	0.463
9	927	02:20	184.32	1.0	8.95	12.80	2.22	1.2	3.46	0.0993	0.195	0.387

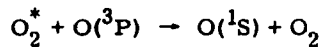
*This calibration is somewhat in doubt.

The dissociative recombination of molecular oxygen,



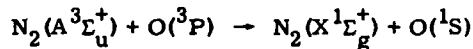
has also been proposed. It requires the formation of O_2^+ first, and then the follow-on reaction with the electrons. A full description requires a non-linear chemistry involving ions of other species as well. Recent estimates of its importance¹² indicate it has a minor role at heights in excess of 100 km.

Finally, we consider the energy transfer from excited electronic states of molecular oxygen and nitrogen. The reaction of ground state atomic oxygen, O^{3P} , with an appropriate electronic state of molecular oxygen, O_2^* , as



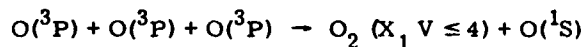
has been proposed by Barth.¹³

The final reaction, the energy transfer from $\text{N}_2(\text{A}^3\Sigma_u^+)$ with O^{3P} , as



is probably the main production source for many auroral conditions.

In addition, there is the steadier background airglow, probably due to the Chapman mechanism, and its variants.^{13, 14}



Following the deposition of energetic electrons there are many excited states of the major atmospheric species created by the primary and secondary electrons. Because of its brightness and short radiative lifetime, a convenient monitor of the temporal behavior of the electron flux is the $\text{N}_2^+(\text{B}^2\Sigma_u^+ \rightarrow \text{X}^2\Sigma_g^+)$ first negative (0-0) band at 3914 Å.

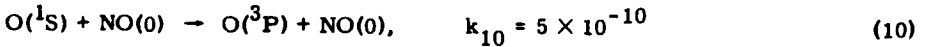
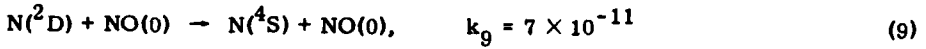
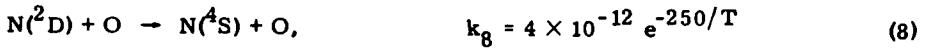
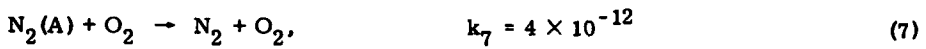
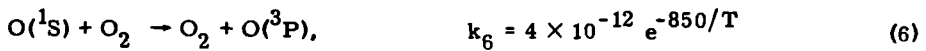
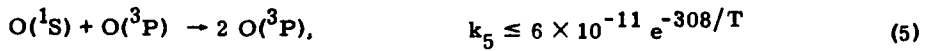
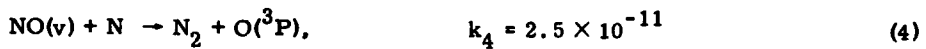
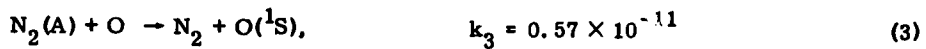
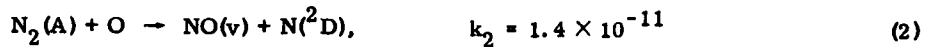
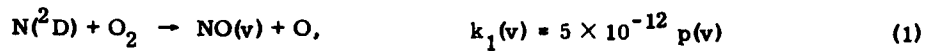
O'Neil¹² has found that it takes 20 ion pairs to produce one 3914 Å photon, so we have a relation between the photon production rate and the ion pair production (about 34.9 ev/ion pair) as

$$\zeta_{3914}(t) = (1/20)\eta(t)$$

-
12. O'Neil, R. R., Lee, E. T. P., and Huppi, E. R. (1979) Auroral O^{1S} production and loss processes: ground based measurements of the artificial auroral experiment PRECEDE, *J. Geophys. Res.* 84:823.
 13. Barth, C. A. (1961) The 5577 Angstrom airglow, *Science* 134:1426.
 14. Chapman, S. (1931) Some phenomena of the upper atmosphere (Bakerian Lecture) *Proc. Roy. Soc. (London)* A 132:353.

where $\zeta_{3914}(t)$ is the 3914 Å photon production rate in photons/sec-cm³, and $\eta(t)$ is the rate of ion pair production (ion pairs/sec-cm³).

The following set of reactions are used to describe the time dependent concentrations of the species N(²D), N₂(A), NO(v), and O(¹S) where we assume a constant background of O₂, N₂, and O.



We also have the radiative decay set,



15. Billingsley, F.P. (1976) Calculated vibration-rotation intensities for NO(X² π)
J. Mol. Spectr. 61:53.

In addition, there is the production for $N(^2D)$ and $N_2(A)$ per ion pair, written as

$\epsilon_{N(^2D)}$ is the production rate for $N(^2D)$ /ion pair. It has a value between 1 and 1.5.

$\epsilon_{N_2(A)}$ is the production rate for $N_2(A)$ /ion pair. It has a value between 0.5 and 1.0.

3.2.2 PREDICTING THE O(^1S) CHEMISTRY

From this reaction set, we may write the rate equation set as:

$$\frac{d}{dt} [N(^2D)] = \epsilon_{N(^2D)} \eta(t) - \{k_1[O_2] + k_8[O] + K_9[NO(0)]\} [N(^2D)] \\ + k_2[O] [N_2(A)]$$

$$\frac{d}{dt} [N_2(A)] = \epsilon_{N_2(A)} \eta(t) - \{k_7[O_2] + (k_2 + k_3)[O] + 0.53\} [N_2(A)]$$

$$\frac{d}{dt} [O(^1S)] = k_3[O] [N_2(A)] - \{k_6[O_2] + k_5[O] + k_{10}[NO(0)] + 1.18\} [O(^1S)]$$

This is a set of coupled linear time invariant first order differential equations, driven by the electron pulse deposition function $\eta(t)$. Such a system is amenable to solution by linear transform methods, especially the Fourier integral transform. The Fourier transform of the derivative $\frac{df(t)}{dt}$ is expressible in terms of the Fourier transform of $f(t)$, as

$$FT \left[\frac{df(t)}{dt} \right] = i\omega F(\omega)$$

Applying the transform to the three rate equations, we have in radian frequency space ω ,

$$\frac{[N(^2D)]_\omega}{\eta(\omega)} = \frac{\epsilon_{N(^2D)}}{i\omega + \alpha} + \frac{k_2[O] [N_2(A)]_\omega}{\eta(\omega)} \frac{N(^2D)}{N(^2D)}$$

$$\frac{[N_2(A)]_\omega}{\eta(\omega)} = \frac{\epsilon_{N_2(A)}}{i\omega + \alpha} \frac{N_2(A)}{N_2(A)}$$

$$\frac{[O(^1S)]_\omega}{\eta(\omega)} = \frac{k_3[O]}{i\omega + \alpha_{O(^1S)}} + \frac{[N_2(A)]}{\eta(\omega)}$$

where the quenching coefficients α are defined as

$$\alpha_{N(^2D)} = \{k_1[O_2] + k_8[O] + k_9[NO(0)]\}$$

$$\alpha_{N_2(A)} = \{h_7[O_2] + (k_2 + k_3)[O] + 0.53\}$$

$$\alpha_{O(^1S)} = \{k_6[O_2] + k_5[O] + k_{10}[NO(0)] + 1.18\}$$

Thus, the transfer function for the ratio of the 5577Å intensity to the 3914Å intensity is

$$\frac{I(\omega)}{5577} / \frac{I(\omega)}{3914} = \frac{A_{5577} k_3[O] e_{N_2(A)}}{\left(\frac{1}{20}\right) \left(i\omega + \alpha_{O(^1S)}\right) \left(i\omega + \alpha_{N_2(A)}\right)}$$

This is a double pole function, which has for the $\omega \rightarrow 0$ limit

$$\frac{\xi(0)}{5577} / \frac{\xi(0)}{3914} = \frac{20(1.18) e_{N_2(A)} k_3[O]}{\alpha_{O(^1S)} \alpha_{N_2(A)}}$$

We observe a pole around 1.2 sec^{-1} , the radiative decay for the $O(^1S)$ state with no quenching. This is consistent with the calculation of $\alpha_{O(^1S)}$ from

$$\alpha_{O(^1S)} = (1.18 + 4 \times 10^{-12} e^{-850/T} [O_2] + 5 \times 10^{-10} [NO])$$

for most altitudes greater than 100 km, and where we ignore oxygen atom quenching in this region, as recent laboratory measurements suggest. We then predict photon ratio values from 1.4 to 4.3 for reasonable values of $[O]$ and $[O_2]$, consistent with the range of our field measurements.

3.2.3 THE $3 \mu\text{m}$ PULSE AND ITS INTERPRETATION AS CHEMILUMINESCENT NITRIC OXIDE

The reaction of $\text{N}^2(\text{D})$ with molecular oxygen produces nitric oxide with a non-thermal vibration distribution.¹⁶ This initial production quickly becomes redistributed by the natural process of radiative decay and collisional reactions with other molecules. The complete radiative cascade process may be described in terms of a set of rate equations of the first order, written in matrix form as

$$\frac{d}{dt} \underline{\underline{N}} = (\underline{\underline{A}}) (\underline{\underline{N}}) + \underline{\underline{P}} - (\underline{\underline{Q}}) (\underline{\underline{N}})$$

where $(\underline{\underline{N}})$ is a column matrix for the NO vibrational levels, and $(\underline{\underline{P}})$ is the time dependent production column matrix whose entries reflect the initial distribution among vibrational levels.¹⁶ The square matrices $(\underline{\underline{A}})$ (Table 9) for radiative cascade and $(\underline{\underline{Q}})$ for collisional quenching use the Einstein values of NO given by Billingsley¹⁵ and values similar to those used by O'Neil.¹² An expanded form of the matrix set is shown in Figure 14 with the production used by Archer⁶ in Table 8.

We treat the general matrix set by performing a Fourier transform with the result

$$(\underline{i\omega I + Q - A}) (\underline{\underline{N}})_\omega = (\underline{\underline{P}})_\omega$$

and we assume that $\underline{\underline{P}} = \eta(t) \underline{\underline{p}}$ where the scalar $\eta(t)$ is the time dependence of the ion pair production used earlier, and $\underline{\underline{p}}$ is the fractional production of Kennealy¹⁶ as used by Archer.⁶ The solution of the nitric oxide vibrational levels then becomes the inversion of a 12×12 matrix acting on $\underline{\underline{p}}$, as

$$(\underline{\underline{N}})_\omega = (\underline{i\omega I + Q - A})^{-1} (\underline{\underline{P}}) \eta(\omega)$$

The predicted NO vibration-rotation band spectra $\underline{\underline{\xi}}$ for a given Δv sequence is then determined by the matrix operation

$$\underline{\underline{\xi}} = \{B(\Delta v)\} (\underline{\underline{N}})$$

where $B(\Delta v)$ is the Einstein coefficient matrix for a given Δv .

16. Kennealy, J. P., DelGreco, F. P., Caledonia, G. E., and Green, B. D. (1978) Nitric oxide chemiexcitation occurring in the reaction between metastable nitrogen atoms and oxygen molecules, *J. Chem. Phys.* 69:1574.

Table 8. Einstein Emission Coefficients $A_{vv'}$ of NO and the Relative Production for the $N(^2D) + O_2$ Reaction (Billingsley)¹⁵

v	$\Delta v=1$ ($v' = v-1$)	$\Delta v=2$ ($v' = v-2$)	$P(v)$
0	0.0	0.0	0.1044
1	10.78	0.0	0.1044
2	20.43	0.46	0.1044
3	29.11	1.51	0.1044
4	36.49	3.10	0.1044
5	42.93	4.90	0.1044
6	48.54	7.29	0.0982
7	53.54	9.63	0.0982
8	57.48	12.50	0.0815
9	60.55	15.68	0.0418
10	62.77	19.14	0.0261
11	64.15	22.94	0.0158
12	64.61	27.15	0.0120

$$\sum_{v=0}^{12} P(v) = 1.0$$

The field measurements use a filter which passes only a fractional amount of each band, so we must form a row filter matrix \underline{F} to give the total radiation $R(\Delta v)$ through the filter as

$$R(\Delta v) = (\underline{F}) (\underline{\xi})$$

The effective filter with atmospheric transmission is designated "Total Transmission" in Table 10.

These operations were modeled using a PDP-8E computer and selected results are shown in the Tables 11 through 14 for the zero frequency limit, $\omega \rightarrow 0$. For the $\Delta v = 2$ band at $3 \mu m$, there are 0.2836 photons/ $\{N(^2D) + O_2\}$ reaction available in the zero quenching limit, but the filter used by the AFGL radiometer

Table 9. Radiative Cascade Matrix

$A =$	-10.78	20.43	1.51	0	0	0	0	0	0	0	0
	0	-20.89	29.11	3.10	0	0	0	0	0	0	0
	0	0	-30.62	36.49	4.90	0	0	0	0	0	0
	0	0	0	-39.59	42.93	7.29	0	0	0	0	0
	0	0	0	0	-47.83	48.54	9.63	0	0	0	0
	0	0	0	0	0	-55.83	53.54	12.50	0	0	0
	0	0	0	0	0	0	-63.17	57.48	15.68	0	0
	0	0	0	0	0	0	0	-69.98	60.55	19.14	0
	0	0	0	0	0	0	0	0	-76.23	62.77	22.94
	0	0	0	0	0	0	0	0	0	-81.91	64.15
	0	0	0	0	0	0	0	0	0	0	-87.09
	0	0	0	0	0	0	0	0	0	0	64.61
	0	0	0	0	0	0	0	0	0	0	-91.76

$$\begin{aligned}
 \frac{d}{dt} \begin{bmatrix} \text{NO(1)} \\ \text{NO(2)} \\ " \\ " \\ " \\ " \\ " \\ " \\ " \\ " \\ \text{NO(12)} \end{bmatrix} &= \begin{bmatrix} -a_{10} & a_{21} & a_{31} & \dots & a_{12,1} \\ 0 & -(a_{21}+a_{20}) & a_{32} & a_{42} & \dots \\ 0 & 0 & -(a_{32}+a_{31}) & a_{43} \cdot a_{53} & \dots \\ " & " & " & " & " \\ " & " & " & " & " \\ " & " & " & " & " \\ " & " & " & " & " \\ 0 & \dots & \dots & \dots & -(a_{12,11}+a_{12,10}) \end{bmatrix} \begin{bmatrix} \text{NO(1)} \\ \text{NO(2)} \\ " \\ " \\ " \\ " \\ " \\ " \\ " \\ \text{NO(12)} \end{bmatrix} \\
 + \begin{bmatrix} p(1) \\ p(2) \\ " \\ " \\ " \\ " \\ " \\ " \\ " \\ p(12) \end{bmatrix} \begin{bmatrix} q(1) & 0 & 0 & \dots \\ 0 & q(2) & 0 & \dots \\ 0 & 0 & q(3) & \dots \end{bmatrix} \begin{bmatrix} \text{NO(1)} \\ \text{NO(2)} \\ " \\ " \\ " \\ " \\ " \\ " \\ " \\ \text{NO(12)} \end{bmatrix} \\
 - [M] \begin{bmatrix} q'(1) & -q'(2) & 0 & 0 & \dots \\ 0 & q'(2) & -q'(3) & 0 & \dots \\ 0 & 0 & q'(3) & -q'(4) & \dots \end{bmatrix} \begin{bmatrix} \text{NO(1)} \\ \text{NO(2)} \\ " \\ " \\ " \\ " \\ " \\ " \\ " \\ \text{NO(12)} \end{bmatrix} \\
 - [M'] \begin{bmatrix} q'(12) \\ \text{NO(12)} \end{bmatrix}
 \end{aligned}$$

Figure 14. The Rate Equations in Matrix Form

Table 10. NO Atmosphere and Filter Transmission

Band	R _{max}	P _{max}	Wavelength (μm)		Filter Transmission	Atmospheric & Filter Transmission	Total Transmission $\frac{R + A \times P}{1 + A}$
			R branch	P branch			
<u>Temperature = 300°K (A = 1.160)</u>							
2-0	2.668	2.760	0.0000	0.0000	0.0000	0.0000	0.0000
3-1	2.708	2.748	0.0000	0.0000	0.0000	0.0000	0.0000
4-2	2.750	2.791	0.0000	0.0095	0.0000	0.0020	0.0011
5-3	2.793	2.835	0.0100	0.3296	0.0027	0.2705	0.1465
6-4	2.837	2.881	0.3536	0.7970	0.2952	0.7704	0.5504
7-5	2.883	2.928	0.7880	0.8801	0.7613	0.8641	0.8175
8-6	2.930	2.977	0.8811	0.9167	0.8676	0.8977	0.8838
9-7	2.979	3.027	0.9151	0.9508	0.8965	0.9349	0.9172
10-8	3.030	3.080	0.9536	0.9859	0.9374	0.9666	0.9531
11-9	3.082	3.134	0.9875	0.7930	0.9676	0.7826	0.8682
12-10	3.136	3.190	0.7587	0.0640	0.7485	0.0609	0.3793
<u>Temperature = 600°K (A = 1.126)</u>							
2-0	2.662	2.716	0.0000	0.0000	0.0000	0.0000	0.0000
3-1	2.702	2.758	0.0000	0.0000	0.0000	0.0000	0.0000
4-2	2.743	2.801	0.0000	0.0254	0.0000	0.0102	0.0054
5-3	2.786	2.846	0.0054	0.4472	0.0008	0.3878	0.2058
6-4	2.830	2.892	0.2716	0.7770	0.2138	0.7565	0.5012
7-5	2.876	2.939	0.8164	0.8946	0.7840	0.8801	0.8349
8-6	2.923	2.989	0.8735	0.9089	0.8565	0.8927	0.8757
9-7	2.972	3.040	0.9180	0.9600	0.8996	0.9428	0.9225
10-8	3.022	3.092	0.9435	0.9941	0.9283	0.9732	0.9521
11-9	3.074	3.147	0.9824	0.5837	0.9638	0.5743	0.7575
12-10	3.128	3.203	0.8625	0.0395	0.8506	0.0313	0.4167

Table 11. NO Overtone {Photons/N(²D) + O₂} Reaction

Quenching Coefficient α for NO(v) + M → NO(0) + M

v - v'	$\alpha(\text{sec}^{-1})$					
	0	1.2	2	4	8	16
2-0	0.0167	0.0145	0.0132	0.0107	0.0074	0.0042
3-1	0.0317	0.0287	0.0269	0.0231	0.0175	0.0112
4-2	0.0421	0.0390	0.0371	0.0330	0.0266	0.0186
5-3	0.0444	0.0419	0.0403	0.0368	0.0310	0.0232
6-4	0.0438	0.0418	0.0406	0.0377	0.0329	0.0260
7-5	0.0376	0.0362	0.0354	0.0334	0.0300	0.0248
8-6	0.0285	0.0277	0.0271	0.0259	0.0237	0.0202
9-7	0.0174	0.0169	0.0166	0.0159	0.0147	0.0127
10-8	0.0111	0.0108	0.0106	0.0103	0.0096	0.0084
11-9	0.0063	0.0062	0.0061	0.0060	0.0056	0.0051
12-10	0.0035	0.0035	0.0034	0.0034	0.0032	0.0030

Table 12. NO Fundamental {Photons/N(²D) + O₂}

Quenching Coefficient α for NO(v) + M → NO(0) + M

v - v'	$\alpha(\text{sec}^{-1})$					
	0	1.2	2	4	8	16
1-0	0.8788	0.7004	0.6085	0.4422	0.2608	0.1222
2-1	0.7426	0.6452	0.5901	0.4788	0.3323	0.1880
3-2	0.6128	0.5542	0.5196	0.4459	0.3389	0.2164
4-3	0.4958	0.4595	0.4375	0.3890	0.3141	0.2191
5-4	0.3896	0.3673	0.3536	0.3226	0.2723	0.2033
6-5	0.2920	0.2788	0.2706	0.2516	0.2197	0.1731
7-6	0.2092	0.2017	0.1970	0.1860	0.1670	0.1378
8-7	0.1312	0.1274	0.1249	0.1192	0.1090	0.0929
9-8	0.0671	0.0654	0.0643	0.0616	0.0568	0.0490
10-9	0.0364	0.0356	0.0350	0.0338	0.0316	0.0278
11-10	0.0178	0.0175	0.0173	0.0168	0.0159	0.0143
12-11	0.0084	0.0083	0.0082	0.0080	0.0077	0.0071

Table 13. NO Overtone {Photons/N(²D) + O₂} Reaction

Quenching Coefficient α for NO(v) + M → NO(v-1) + M

v - v'	$\alpha(\text{sec}^{-1})$					
	0	1.2	2	4	8	16
2-0	0.0167	0.0158	0.0152	0.0141	0.0121	0.0096
3-1	0.0317	0.0306	0.0299	0.0282	0.0254	0.0212
4-2	0.0421	0.0409	0.0402	0.0384	0.0354	0.0305
5-3	0.0444	0.0434	0.0428	0.0412	0.0385	0.0340
6-4	0.0438	0.0430	0.0424	0.0411	0.0388	0.0348
7-5	0.0376	0.0369	0.0365	0.0355	0.0337	0.0306
8-6	0.0285	0.0281	0.0278	0.0271	0.0258	0.0236
9-7	0.0174	0.0171	0.0170	0.0166	0.0159	0.0146
10-8	0.0111	0.0109	0.0108	0.0106	0.0102	0.0094
11-9	0.0063	0.0063	0.0062	0.0061	0.0059	0.0055
12-10	0.0035	0.0035	0.0034	0.0034	0.0032	0.0030

Table 14. NO Fundamental {Photons/N(²D) + O₂} Reaction

Quenching Coefficient α for NO(v) + M → NO(v-1) + M

v - v'	$\alpha(\text{sec}^{-1})$					
	0	1.2	2	4	8	16
1-0	0.8788	0.7916	0.7425	0.6429	0.5070	0.3566
2-1	0.7426	0.7033	0.6794	0.6262	0.5414	0.4264
3-2	0.6128	0.5908	0.5770	0.5451	0.4909	0.4097
4-3	0.4958	0.4821	0.4734	0.4529	0.4170	0.3599
5-4	0.3896	0.3808	0.3752	0.3618	0.3377	0.2980
6-5	0.2920	0.2864	0.2828	0.2742	0.2584	0.2317
7-6	0.2092	0.2056	0.2033	0.1978	0.1877	0.1702
8-7	0.1312	0.1292	0.1279	0.1247	0.1188	0.1086
9-8	0.0671	0.0662	0.0656	0.0641	0.0614	0.0566
10-9	0.0364	0.03594	0.0356	0.0348	0.0334	0.0310
11-10	0.0178	0.0176	0.0175	0.0171	0.0165	0.0154
12-11	0.0084	0.0083	0.0082	0.0080	0.0077	0.0071

gives only 0.1201 photons/ $\{N(^2D) + O_2\}$ reaction and 0.0812 photons/ $\{N(^2D) + O_2\}$ reaction when the NO quenching coefficient is 16 sec^{-1} . The photon yield per $N(^2D) + O_2$ reaction as a function of quenching coefficient in sec^{-1} is shown in Figure 15 for the $\Delta V = 2$ overtone band and in Figure 16 for the fundamental band.

Thus, the photon ratio for the $3 \mu\text{m}$ to 3914\AA radiation may be written in the zero quenching limit for 100 percent transmission through the filter as

$$\begin{aligned}\mathcal{E}_{NO}/\mathcal{E}_{3914} &= \frac{(0.2836)}{(1/20)} \left\{ \frac{k_1 [O_2] \Sigma}{k_1 [O_2] + k_8 [O]} N(^2D) \right\} \\ &= \frac{(5.672) \epsilon_{N(^2D)}}{1 + (0.8 e^{-250/T}) \left[\frac{[O]}{[O_2]} \right]}\end{aligned}$$

For $\epsilon_{N(^2D)} = 1.5$, the ratio approaches 8.5 for altitudes between 90 km and 115 km.

4. CONCLUSIONS

Data acquired by the narrow-field radiometer and photometer flown at auroral latitudes in April 1979, September 1979, and August 1980 represent a significant improvement in spatial/temporal resolution of measurements on auroral-particle excited air. The low background level and increased sensitivity of the liquid nitrogen cooled SWIR radiometer increases electrical bandwidth by a factor of 300 and reduces the field of view by a factor of 30 as compared to the wide-field instrument (with warm optics) used in earlier flight series.²

Results from a systematic evaluation of 15 data segments, each representing typically 2-3 minute observations on IBC II⁺ aurora of various forms, show statistically significant variability of a factor of 2 in "equilibrium" chemiluminous yield. The mean energy efficiency of approximately 1 percent (if the radiation is NO overtone) derived from the slopes of least-squares fits to the data, is somewhat higher than that inferred from both the laboratory data (0.45 percent) and earlier aircraft measurements.³ Additionally, some of the SWIR radiance enhancements have comparatively longer rise- and fall-times (of up to 5 seconds) than the corresponding 3914\AA traces, while others show no visually detectable offset.

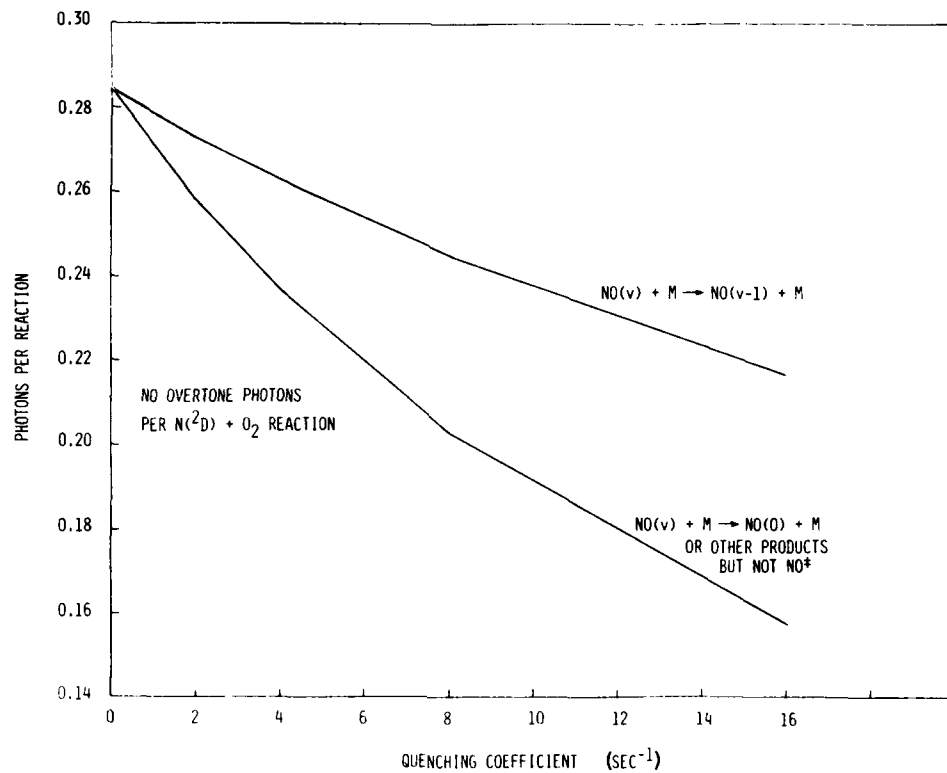


Figure 15. NO Overtone Photons per $N(^2D) + O_2$ Reaction

Since the inferred chemiluminous yield appears to change within individual flights (as well as among flight series) it is unlikely that the variability is an artifact of the instrument response or calibration.

Some evidence exists which suggests that "column integrated" efficiencies may depend on the altitude at which precipitating electrons deposit their energy (Figures 6 and 7) as might be expected from the increased quenching of NO^+ by O at lower altitudes. However, the trend inferred from the data set indicates that the mean yield is much more sensitive to altitude than is reasonably predicted from first principles.

No statistically significant correlation with other auroral (or measurement) parameters is apparent in the data. Although preliminary reduction of some of the narrow-field data seemed to indicate a trend towards higher mean yields in solar illuminated aurora, the results from the expanded data base presented here do not support this finding.

The high spatial resolution of the radiance measurements show the SWIR column emission to be closely correlated with air fluorescence (to at least

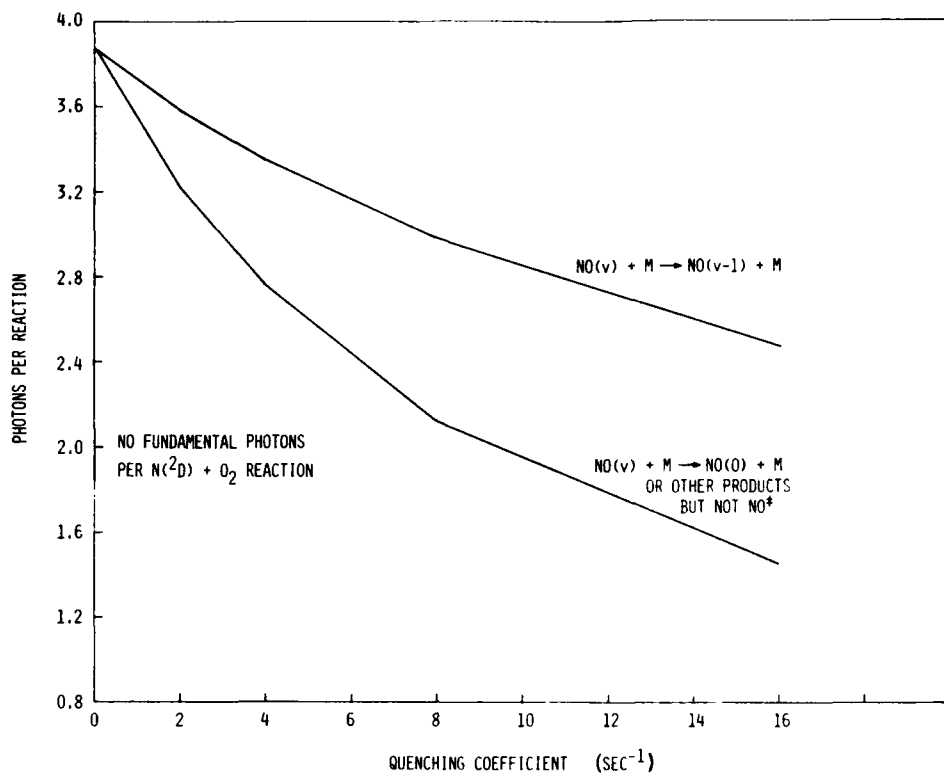


Figure 16. NO Fundamental Photons per N^2D + O_2 Reaction

5 seconds and in some cases less) both when the aurora is pulsating and when stable arcs are scanned by the aircraft's forward motion. Thus, the aerochemical reactions that excite 2.8 – 3.1 μm band output can be said to "follow" the initial energy input to within a few km.

References

1. Kofsky, I. L., Villanucci, D. P., and Sluder, R. B. (1977) Data Reduction and Auroral Characterizations for ICECAP III, HAES Report No. 59, DNA 4220F.
2. Huppi, R. J., and Reed, J. W. (1977) Aircraft Borne Measurements of Infrared Enhancements During ICECAP 1975 and 1976, AFGL-TR-77-0232, AD A051 454.
3. Kofsky, I. L., Villanucci, D. P., and Andrus, W. S. (1978) Assessment of Rocketborne and Airborne Infrared Data, DNA 4731F.
4. Kofsky, I. L., and Villanucci, D. P. (1979) Further Assessment of Infrared Data from Aircraft and Rocket Probes, DNA 5127F.
5. Sluder, R. B., Andrus, W. S., and Kofsky, I. L. (1979) Aircraft Program for Target, Background, and Sky Radiance Measurements, AFGL-TR-79-0139, AD A076 959.
6. Archer, D. H. (1979) Requirements for Improved Infrared Prediction Capability, HAES Report No. 78, DNA 4585F.
7. Huppi, R. J. (1977) A versatile radiometer for infrared emission measurements of the atmosphere and targets, Opt. Eng. 16:485.
8. Kofsky, I. L., Villanucci, D. P., and Sluder, R. B. (1980) Evaluation of Infrared Simulation Data, Final Report for Contract DNA 001-80-C-0010.
9. Sluder, R. B., Andrus, W., Kofsky, I. L., and Villanucci, D. P. (Photometrics, Inc.) Private communication.
10. Rees, M. H., and Luckey, D. (1974) Auroral electron energy derived from ratio of spectroscopic emissions, J. Geophys. Res. 79:5181.
11. Bruce, M., and Eastman, C. (1981) Frequency Analysis of Visible and Infrared Auroras, Utah State University Report No. EDL-SRL-81-4.
12. O'Neil, R. R., Lee, E. T. P., and Huppi, E. R. (1979) Auroral O(¹S) production and loss processes: ground based measurements of the artificial auroral experiment PRECEDE, J. Geophys. Res. 84:823.

13. Barth, C. A. (1961) The 5577 Angstrom airglow, Science 134:1426.
14. Chapman, S. (1931) Some phenomena of the upper atmosphere (Bakerian Lecture) Proc. Roy. Soc. (London) A132:353.
15. Billingsley, F. P. (1976) Calculated vibration-rotation intensities for NO($X^2\pi$) J. Mol. Spectr. 61:53.
16. Kennealy, J. P., DelGreco, F. P., Caledonia, G. E., and Green, B. D. (1978) Nitric oxide chemiexcitation occurring in the reaction between metastable nitrogen atoms and oxygen molecules, J. Chem. Phys. 69:1574.

Appendix A

Data Samples

This appendix contains 15 samples of data which were measured during flights in 1979 and 1980 with the SWIR radiometer, narrow field photometer and NIR radiometer. The date, time and flight number of the 15 samples are listed in Table A1. Table A1 also contains much additional information which has been discussed completely in Section III of this report. The table is reprinted here for convenience. The case numbers correspond to case numbers referred to in other sections of this report.

Each sample of data contains the time history of radiation measured at $3 \mu\text{m}$ with the SWIR radiometer, $1.7 \mu\text{m}$ with the NIR and 3914\AA and 5577\AA measured with the narrow field photometer. The data plots are followed by a sequence of all-sky photos taken during the data sample. Relative to the all-sky photos, the aircraft is moving from left to right and the region of the photo being viewed by the optical instrumentation is slightly right of center.

In Cases 11 through 15 all channels were viewing along the same line of sight. In Cases 1 through 9 the $1.7 \mu\text{m}$ channel (NIR radiometer) was viewing 15° aft of the $3 \mu\text{m}$, 3914\AA and 5577\AA channels. Case 10 is missing since, for some reason, the magnetic tape recorder did not function during this time. In Case 1 the calibration of the 3914\AA channel is somewhat in doubt.

The frequency response of the data processing channels was kept as close to identical as possible. All channels were recorded on FM magnetic tape having a frequency response of 2500 Hz. During data reduction, the $3.7 \mu\text{m}$ and $1.7 \mu\text{m}$

Table A1. Auroral and Observation Parameters During SWIR Enhancements

FLIGHT #/DATE CASE NORTHERN PASSAGE	TIME (Z)	A/C POSITION Lat. Long.	HEADING True Mag.	TRAJECTORY Azimuth (degrees)	DECINATION (Degrees)	SOLAR ANGLE (not 13 deg corrected) (1 = 13.86°)	HEIGHT (km)	MAGNETIC INDEX** (Kp)	PEAK ALTITUDE*** (km)	
									SOLAR ANGLE (13 deg corrected)	MAGNETIC INDEX** (Kp)
1 909/23Apr'79 1158 IMP	0248 0230:20 0230:25	52.89 52.99 52.99	67.06 66.95 66.95	007 029 012	321 321 321	360 331 331	13.61 13.30 13.30	-10.98 D -10.82 D -10.82 D	-10.75 -10.59 -10.59	11.1/14.9 10.9/18.3 10.9/18.3
2 909/23Apr'79 0240	0237	61.36 61.63	71.30 71.76	007	325	360	13.89	-12.14 D -12.02 D	-11.91 -11.79	13.9/18.3 13.6/1.2
3 0213 0216	0213 0216	58.90 59.22	68.67 68.93	325 325	360	338	13.89	-12.02 D	-11.79	13.9/18.3 13.9/1.2
4 0220 0224	0220 0224	58.54 60.87	69.20 69.67	325 325	360	338	13.89	-11.89 D -11.66 D	-11.71 -11.43	13.6/1.3 12.8/0
5 0258 0259	0258 0259	61.76 61.65	69.61 69.26	144 144	180	155	13.51	-12.08 D -12.08 D	-12.31 -12.09	14.6/5 16.1/6
6 908/23Apr 1158	0637 0640	47.00 47.36	67.54 67.66	340	360	344	13.91	-23.42 D -22.89 D	-23.28 -22.75	531/1 507/2
7 928/18Sep 1154	0019 0019	58.26 58.20	73.57 74.12	316 300	279	279	2.19	-9.42 D -9.55 D	-9.16 -9.34	82.5/6 95.5/5
8 928/25Sep 1152	0016 0022	58.04 57.32	77.67 78.02	264 171	292 168	265* 198	-0.54	-12.08 D -12.84 D	-9.83 -11.94	9.4/7 117.3
9 927/27Sep 1151	0230 0223	54.77 55.05	68.83 69.13	327 330	356 360	327 330 "turns"	-1.35	-30.75 D -30.62 D	-30.47 -30.40	9.0/9 905.7
10 928/29Sep 1151	0119 0123	57.10 56.76	76.59 77.27	230 230	260 260	228 228	-2.11	-20.21 D -20.53 D	-20.13 -20.45	4.5/11.8 4.0/11.8
11 023/07Aug'80 1206	0634 0704	62.99 63.34	122.02* 124.75	284 284	252 252	28b 286	16.36	-9.12 D -8.75 D	-8.99 -8.62	79.2/2 72.8
12 028/1Aug'80 1204	1125 1126	65.06 65.16	147.49* 147.36	029 029	360 360	030 030	2.97	-10.10 D -9.95 D	-10.10 -9.70	100.0/106 97.0
13 1159 1203	1159 1203	64.36 63.93	148.43* 148.95	209 209	177 177	207 207	12.96	-9.31 D -9.61 D	-9.31 -9.61	84.9/1.2 90.5/1.2
14 027/19Aug 1204	1024	64.30	148.42*	026	358	029	12.65	-12.89 D -12.34 D	-12.89 -12.34	162/6 149/2
15 1035 1109	1030 1109	65.05 63.88	147.46*	212 212	179 179	208 209	12.65	-11.45 D -11.21	-12.13 -12.13	128.5/5 128.5/5
								<100/47.8 <100/47.8	119.5/4 119.5/4	119.5 119.5

* After flight 023, refers to latitude/longitude of intercept at 120 km of the 13° tilted instruments

** 12-channel photometer readings at maximum auroral column brightness; In zenith in flights 909, 908 and 907
Bracketed values are from narrow-field photometer

*** K's refer to Collage, AK section

• Aircraft is turning to S 0015:30 - 0017:56

signals were demodulated with a lock-in amplifier having a 12 db/octave filter and a time constant setting of $T = 4$ msec. This gives a complex frequency response given by

$$A(f) = \frac{f_0^2}{(f_0 + if)^2} \quad (A-1)$$

where $f_0 = \frac{1}{2\pi T} = 39.79$ Hz. The data was then sampled at 0.01 second intervals. When the data was plotted, a running average of 11 samples was taken to make one plotted data point. The running average effectively convolves the data with a rectangular function which has a width of 0.11 sec. The resulting frequency response is given by

$$B(f) = \frac{\sin \pi Tf}{\pi Tf} \quad (A-2)$$

where $T = \text{averaging time} = 0.11$ sec. The total frequency response is the product of A-1 and A-2

$$H(f) = \frac{f_0^2}{(f_0 + if)^2} \cdot \frac{\sin \pi Tf}{\pi Tf} \quad (A-3)$$

Substituting $f_0 = 39.79$ Hz, $T = 0.11$ sec into A-3, $H(f)$ has a magnitude of 0.707 at $f = 3.97$ Hz.

The narrow field photometer signals were processed in an essentially identical manner. However, since the photometer signals were DC coupled and did not require demodulation, they were filtered by a 2 pole filter which had a rise time matched to that of the lock in amplifier used with the 3 μ m and 1.7 μ m signals.

Equation A-3 gives the frequency response of the plotted data to temporal variations in the aurora. The response of the sensors to spatial variations is somewhat influenced by the temporal response but is dominated by the field of view of the sensors. For a 0.36° by 0.36° field of view and assuming a range from the aircraft to the aurora of 110 km, the sensor would view a section of the aurora 0.69 by 0.69 km. Assuming an aircraft velocity of 430 nmi/h (0.221 km/sec), one field of view is traversed in 3.12 sec. The spatial frequency response is then given by

$$G(f) = \frac{f_1^2}{(f_1 + if)^2} \cdot \frac{\sin \pi L_1 f}{\pi L_1 f} \cdot \frac{\sin \pi L_2 f}{\pi L_2 f} \quad (A-4)$$

where

$$f = \text{cycles per kilometer}$$

$$f_1 = 179.8 \text{ c/km}$$

$$L_1 = 0.0243 \text{ km}$$

$$L_2 = 0.69 \text{ km}$$

$G(f)$ is dominated by the last term which has its first zero at 1.45 c/km.

The variations observed in the data sample could be either the result of temporal variations or spatial variations which result in a time varying signal when scanned by the motion of the aircraft. A detailed effort to separate the temporal variations from the spatial variations has not been performed, but the television and all sky television tend to indicate that the variations are primarily temporal.

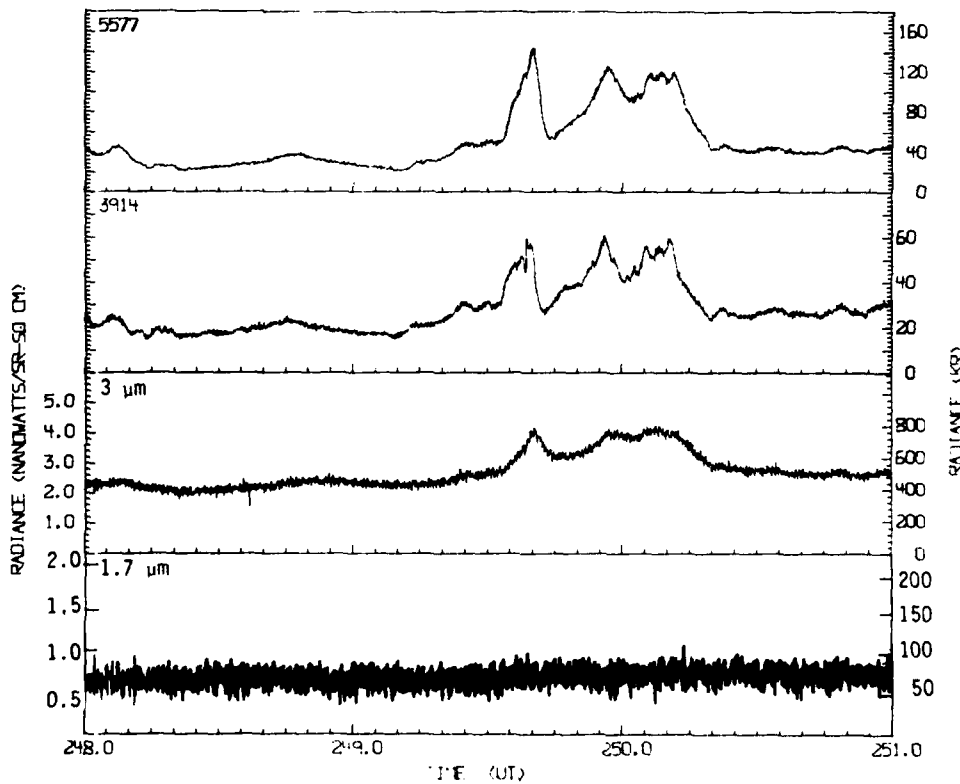


Figure A1. Case 1, Flight 907, 23 April 1979

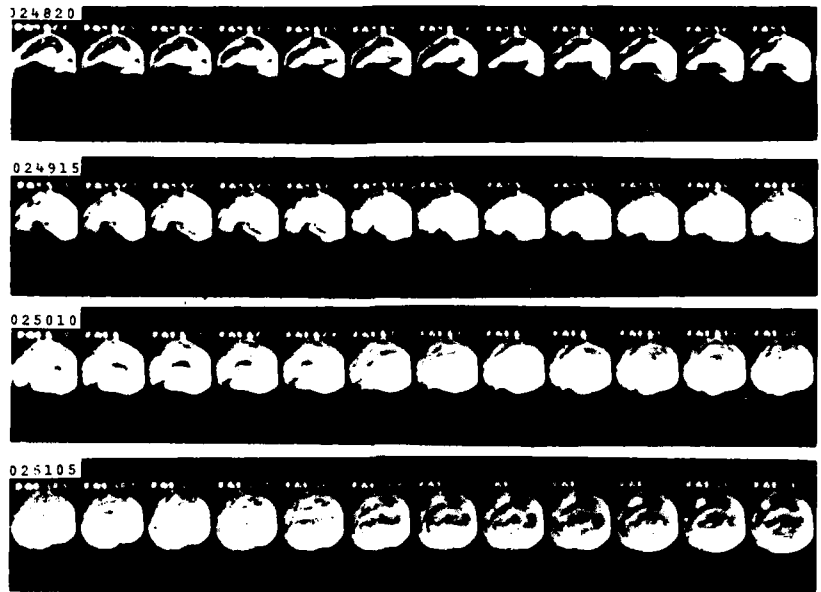


Figure A2. All-Sky Photographs for Case 1, Flight 907, 23 April 1979. Total field of view is 165° . The aircraft motion is from left to right with the instruments viewing a small region slightly right of center. Each exposure is 4.5 seconds

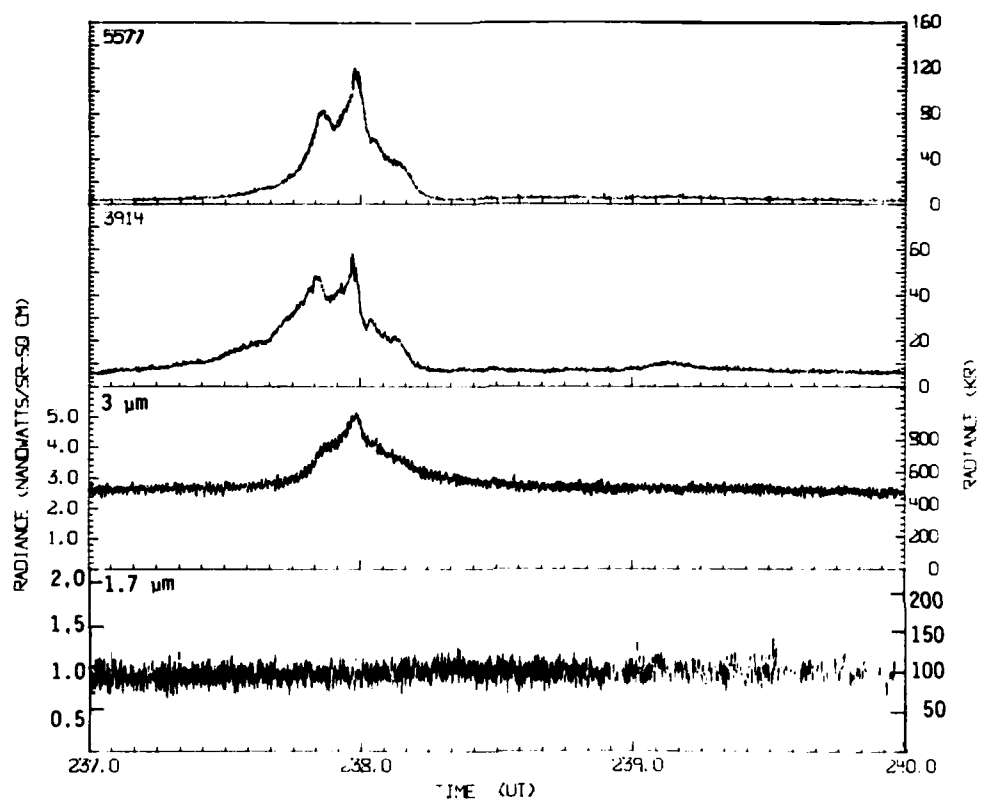


Figure A3. Case 2, Flight 909, 27 April 1979

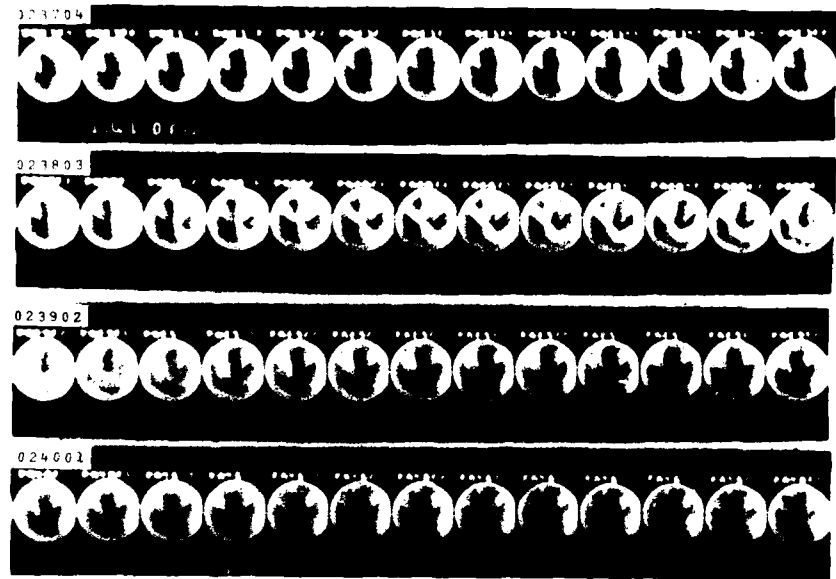


Figure A4. All-Sky Photographs for Case 2, Flight 909, 27 April 1979

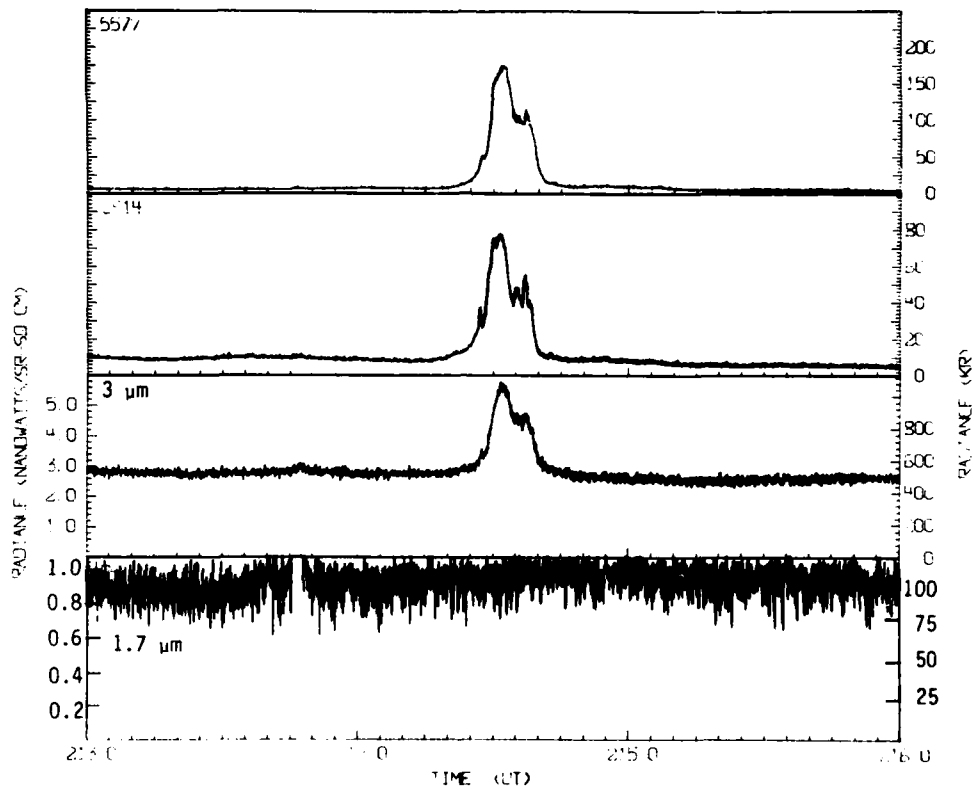


Figure A5. Case 3, Flight 909, 27 April 1979

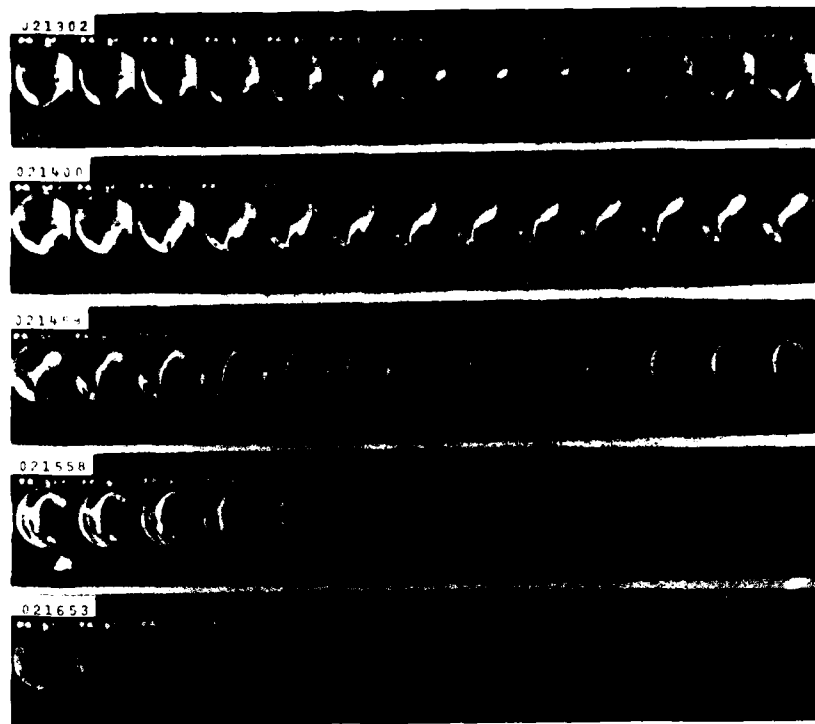


Figure A6. All-Sky Photographs for Case 3, Flight 909, 27 April 1979

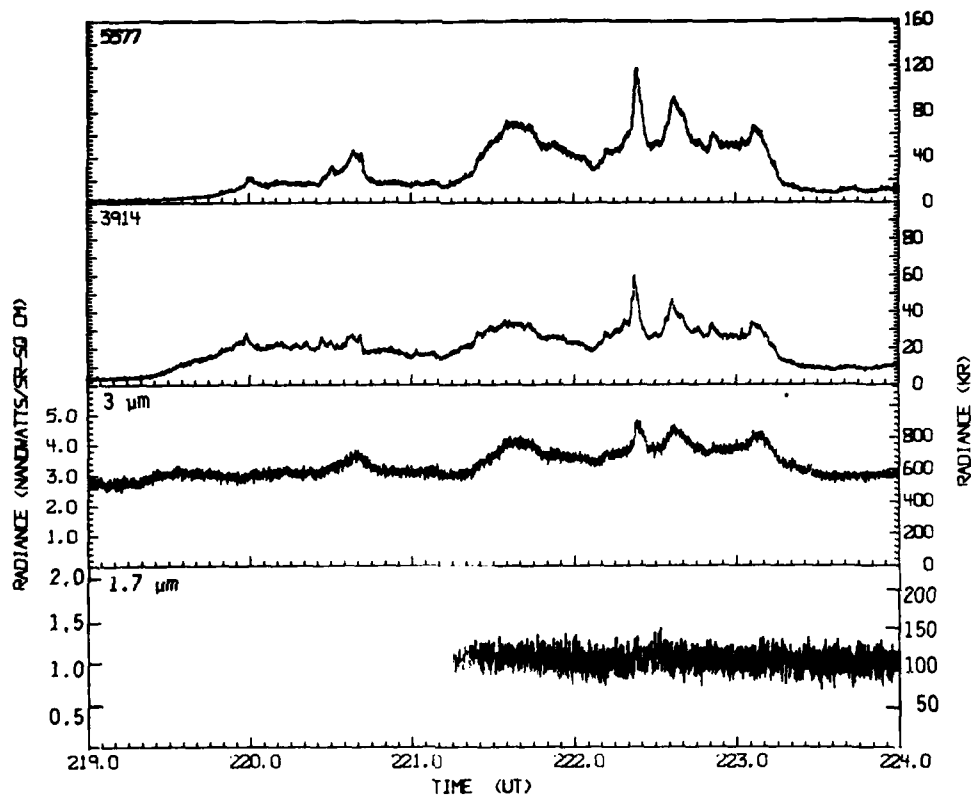


Figure A7. Case 4, Flight 909, 27 April 1979

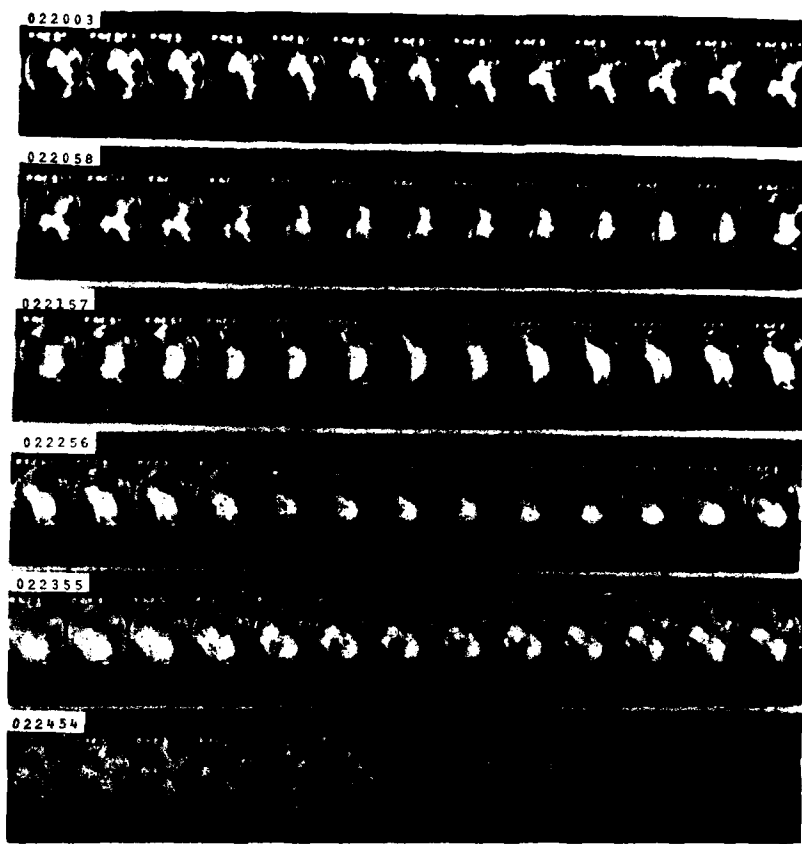


Figure A8. All-Sky Photographs for Case 4, Flight 909, 27 April 1979

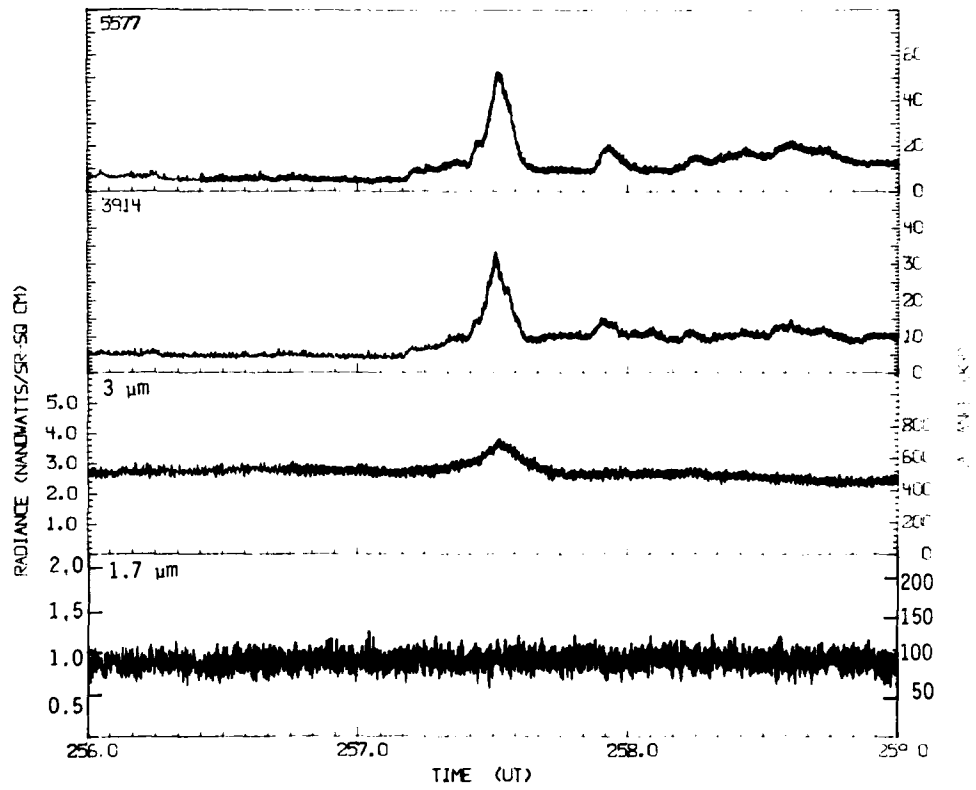


Figure A9. Case 5, Flight 909, 27 April 1979

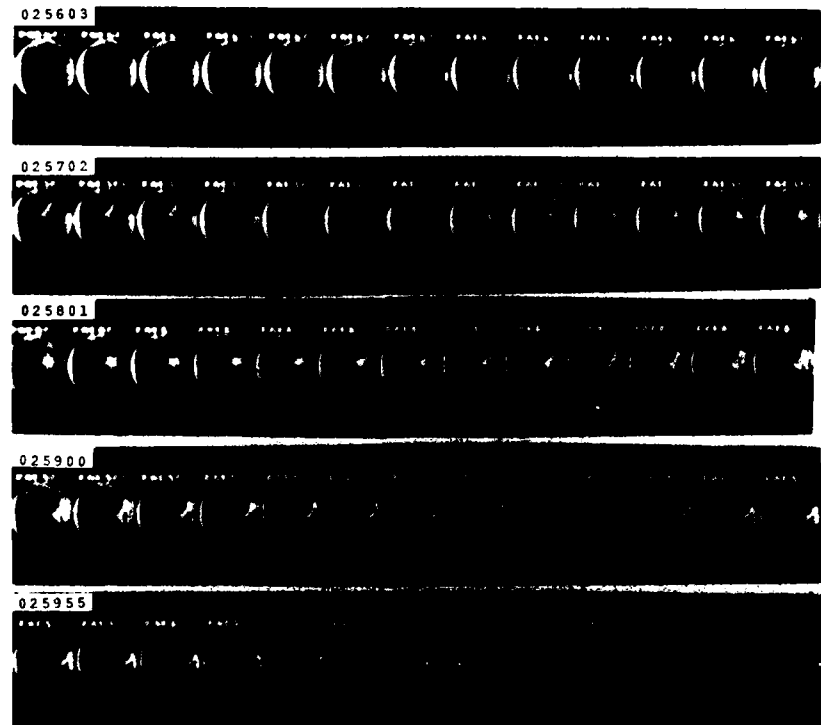


Figure A10. All-Sky Photographs for Case 5, Flight 909, 27 April 1979

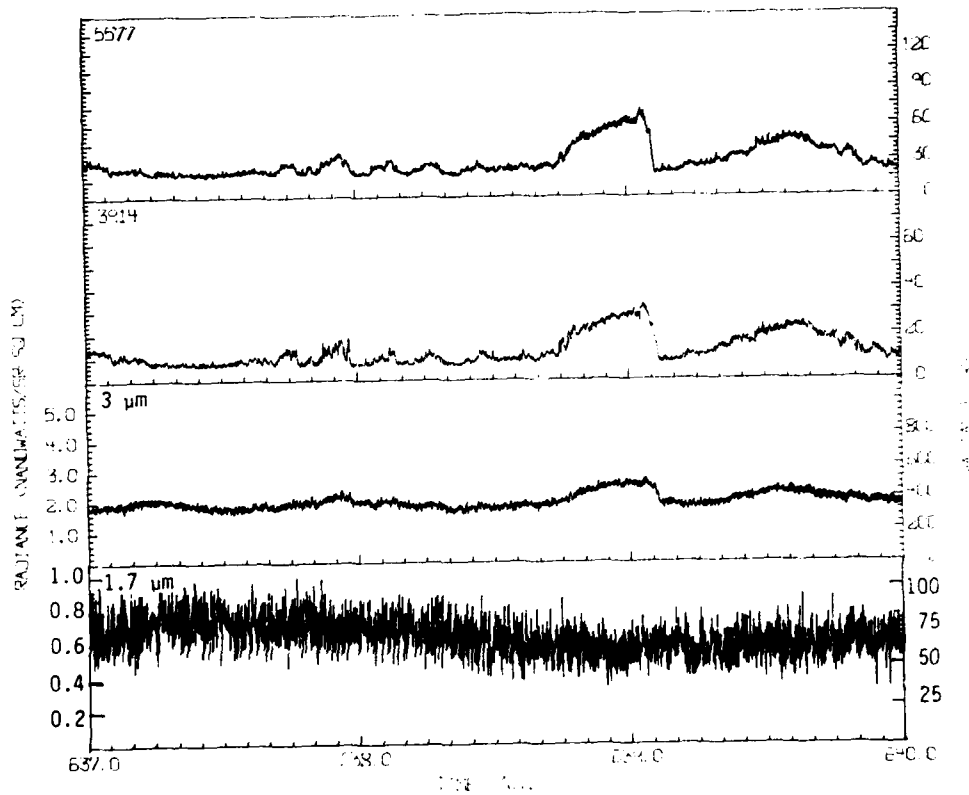


Figure A11. Case 6, Flight 908, 25 April 1979

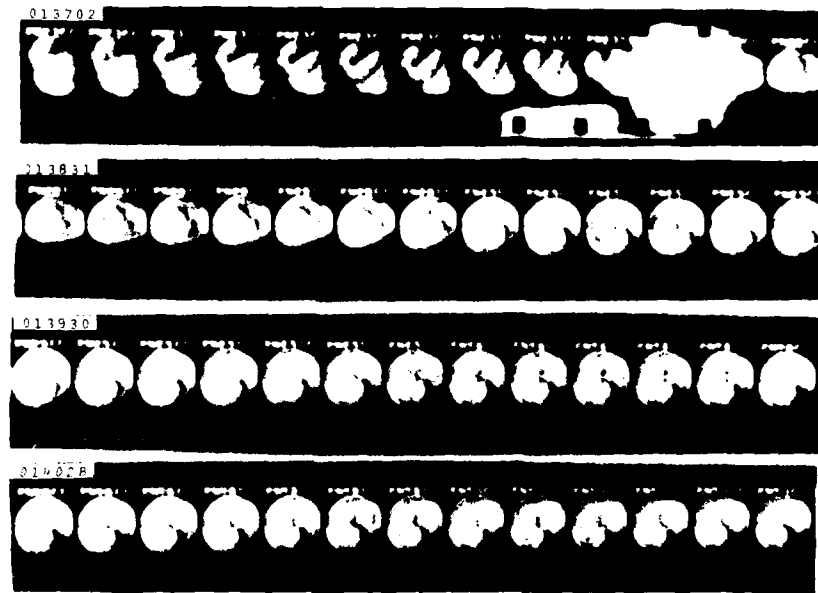


Figure A12. All-Sky Photographs for Case 6, Flight 908, 25 April 1979

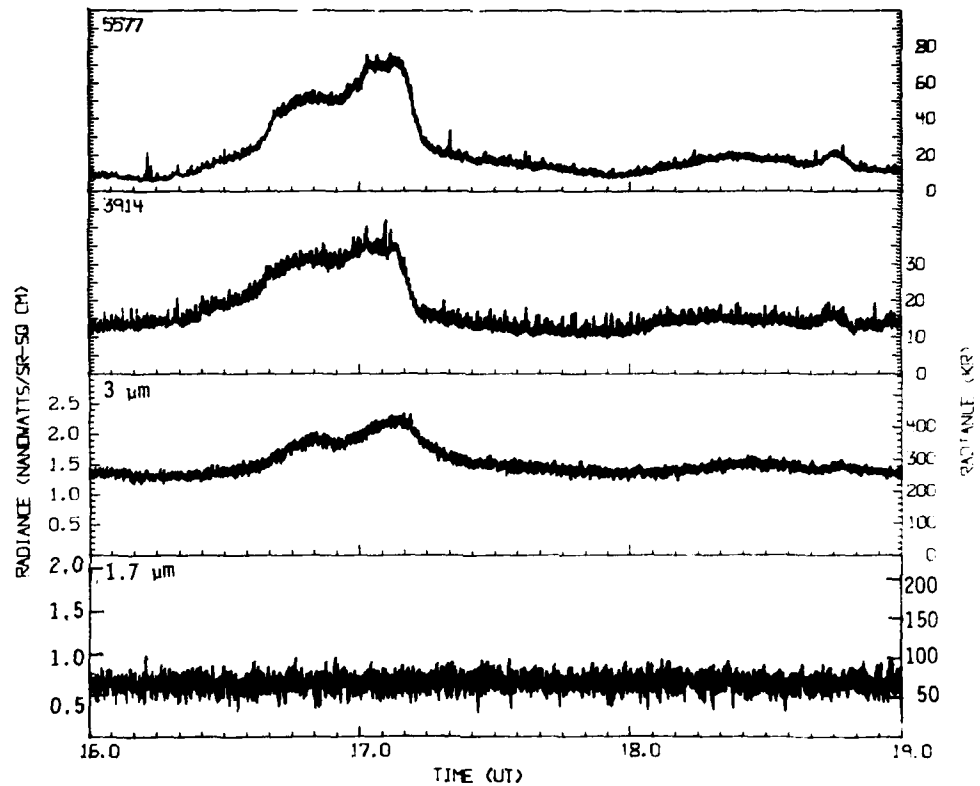


Figure A13. Case 7, Flight 924, 18 September 1979

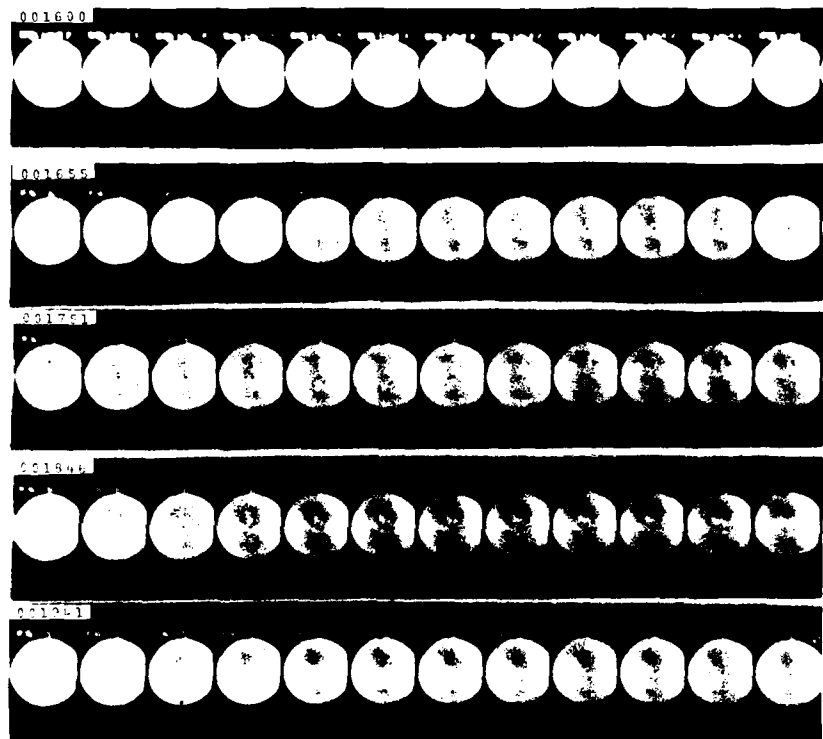


Figure A14. All-Sky Photographs for Case 7, Flight 924, 18 September 1979

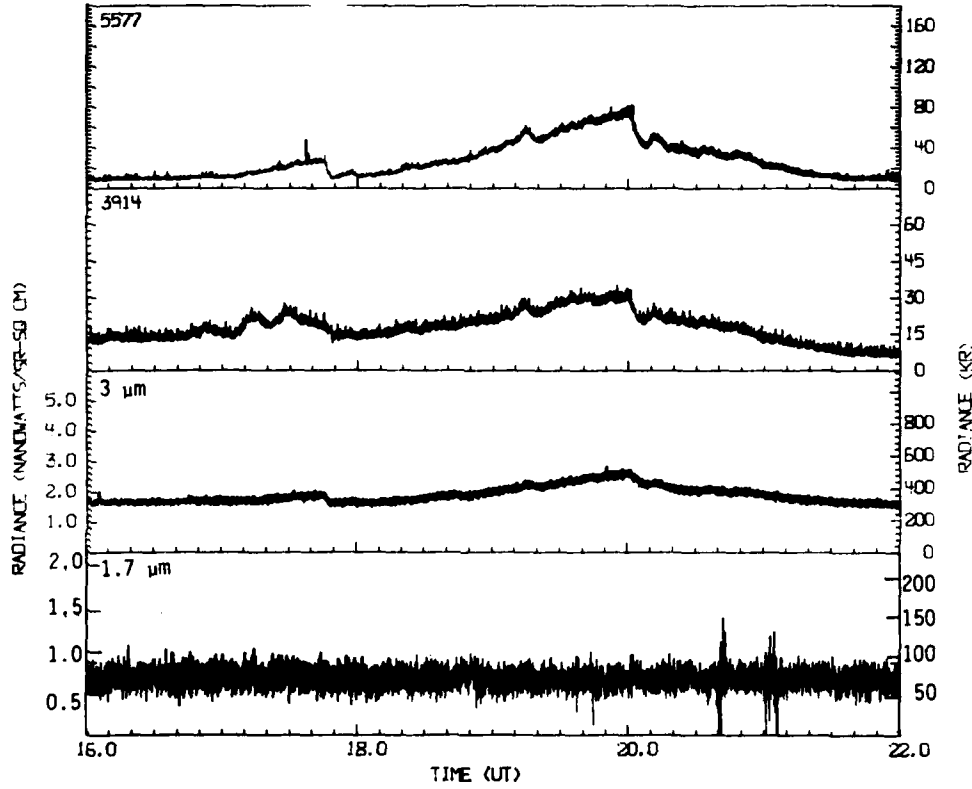


Figure A15. Case 8, Flight 926, 25 September 1979

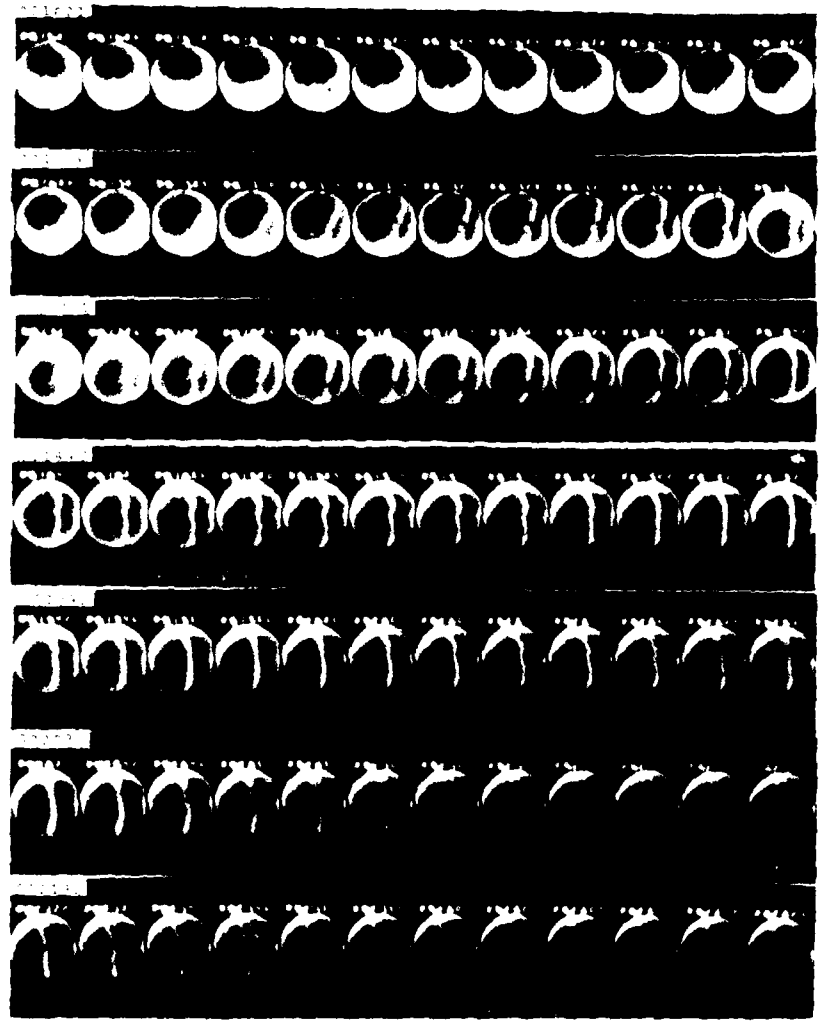


Figure A16. All-Sky Photographs for Case 8, Flight 926, 25 September 1979

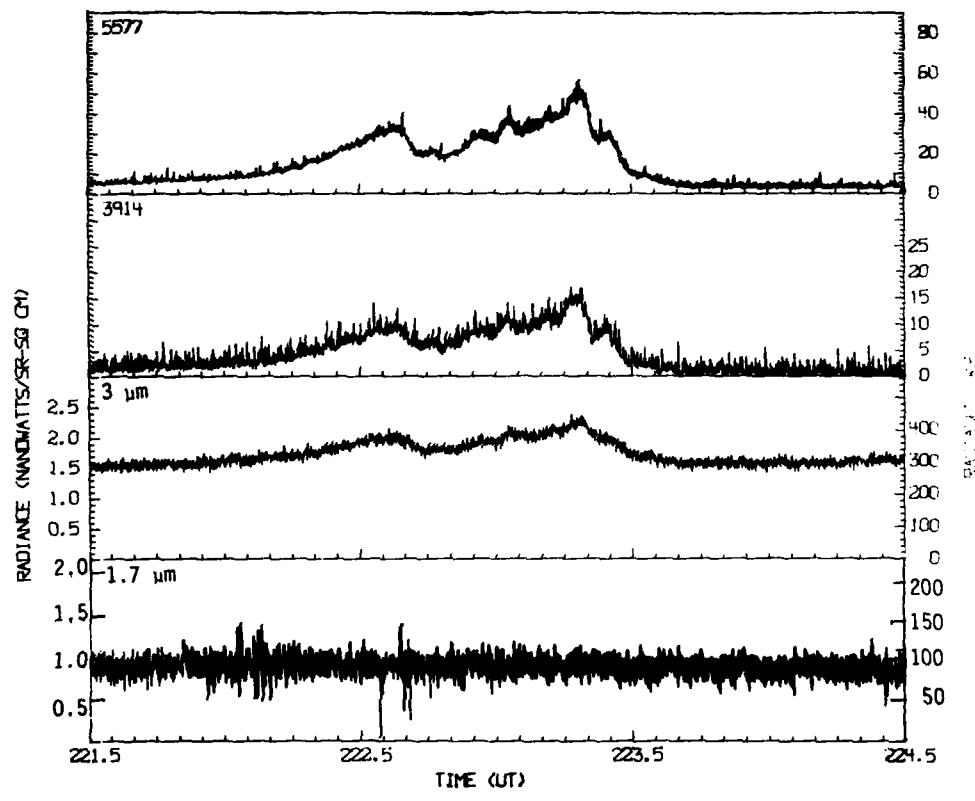


Figure A17. Case 9, Flight 927, 27 September 1979

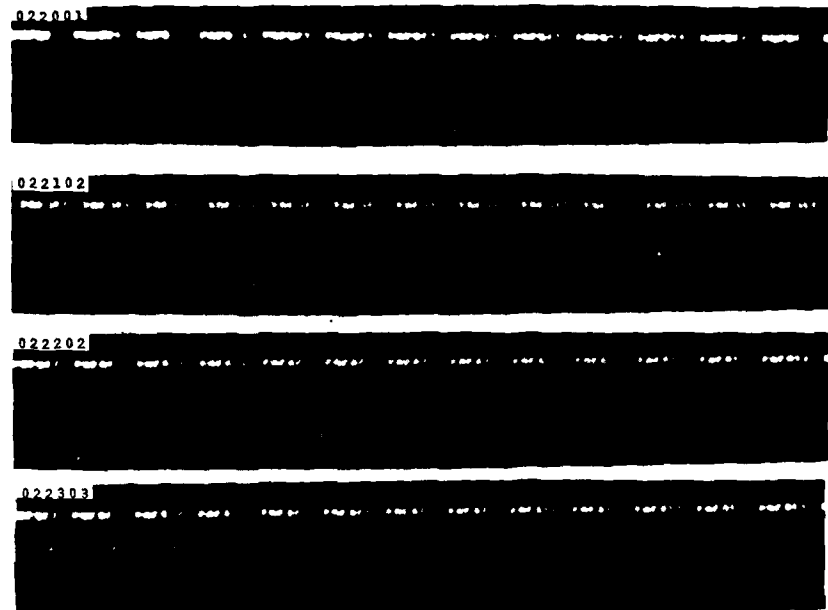


Figure A18. All-Sky Photographs for Case 9, Flight 927, 27 September 1979

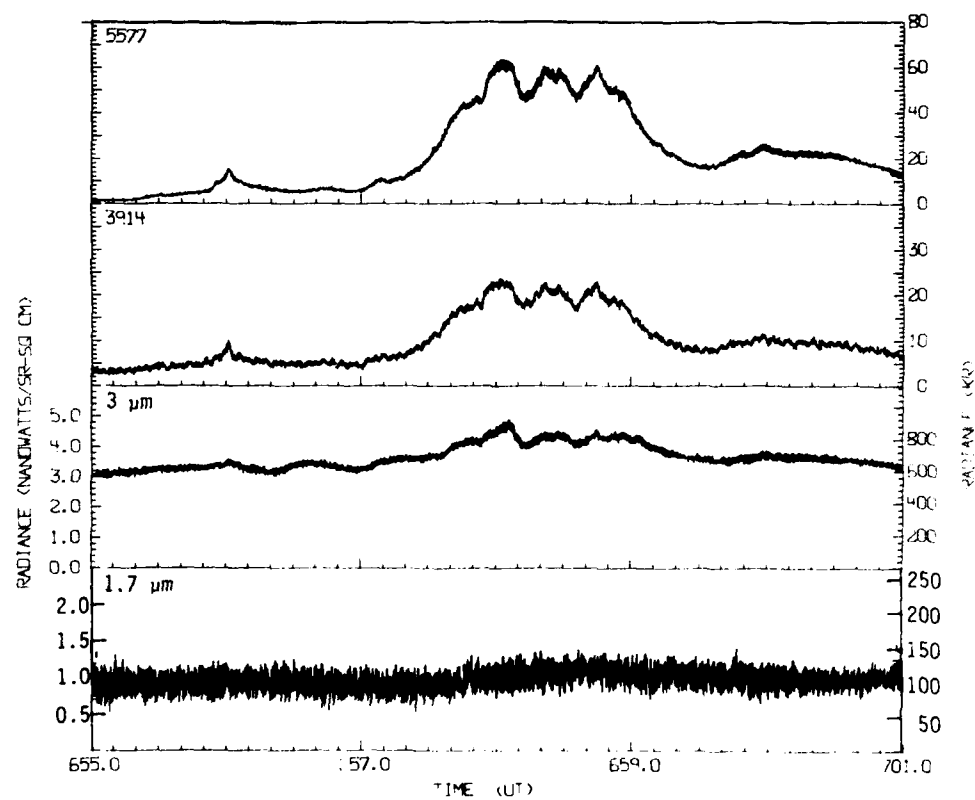


Figure A19. Case 11, Flight 023, 7 August 1980

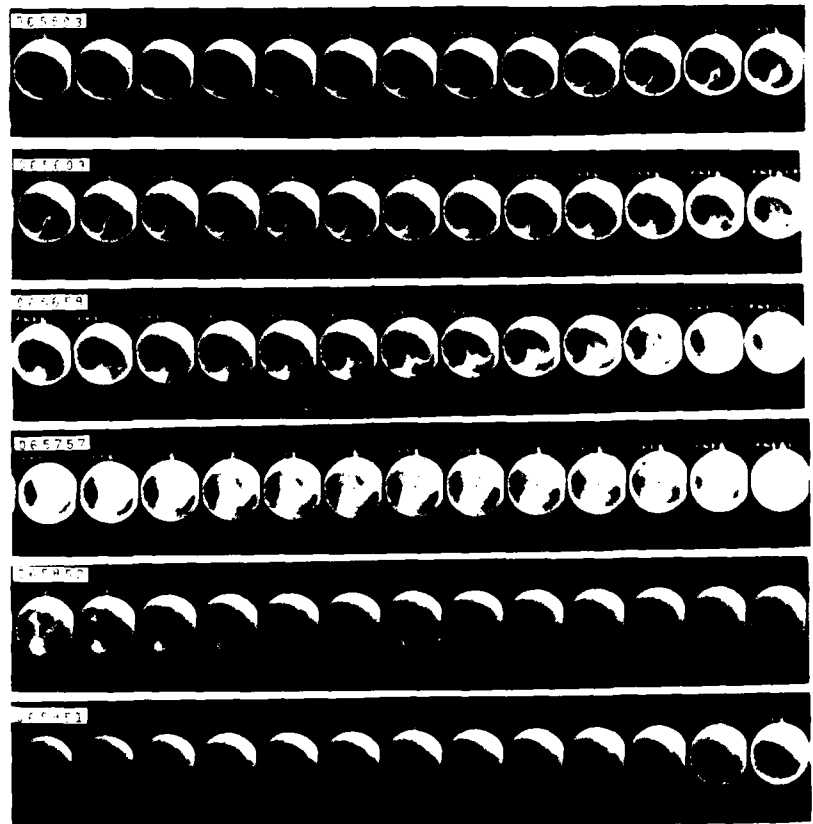


Figure A20. All-Sky Photographs for Case 11, Flight 023, 7 August 1980

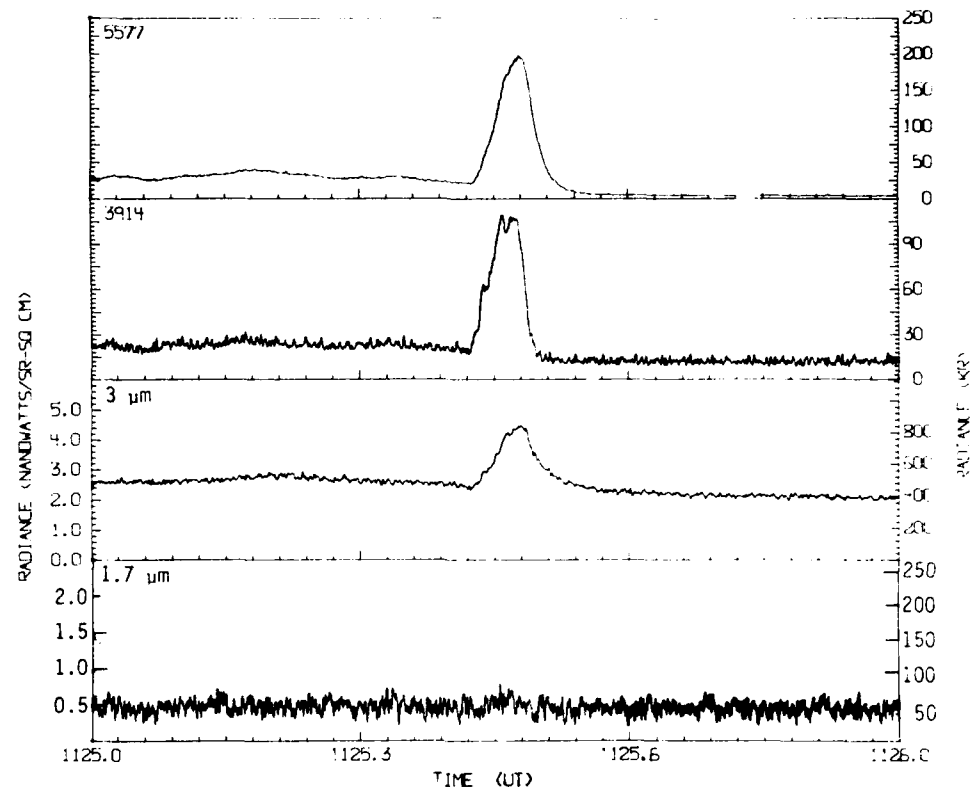


Figure A21. Case 12, Flight 026, 18 August 1980

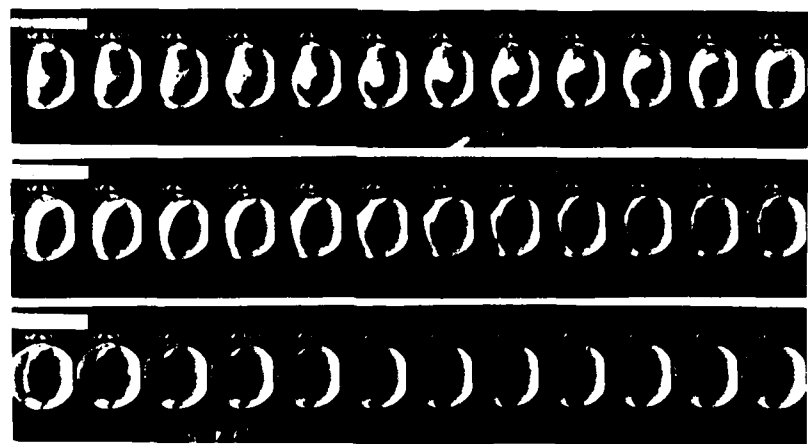


Figure A22. All-Sky Photographs for Case 12, Flight 026, 18 August 1980

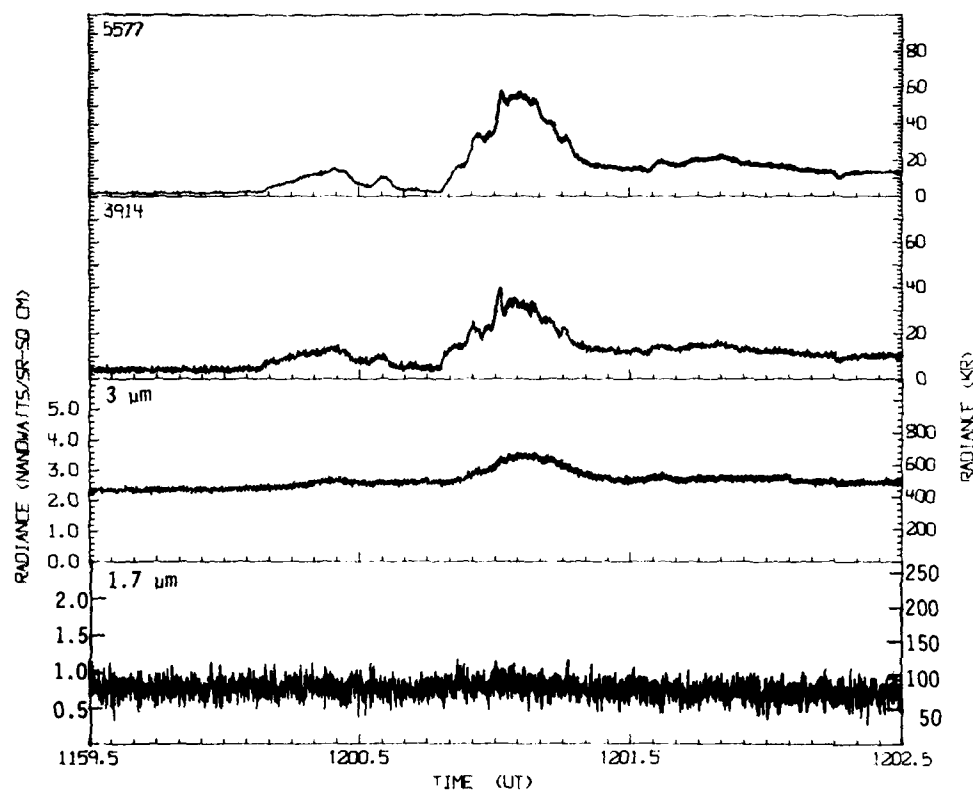


Figure A23. Case 13, Flight 026, 18 August 1980

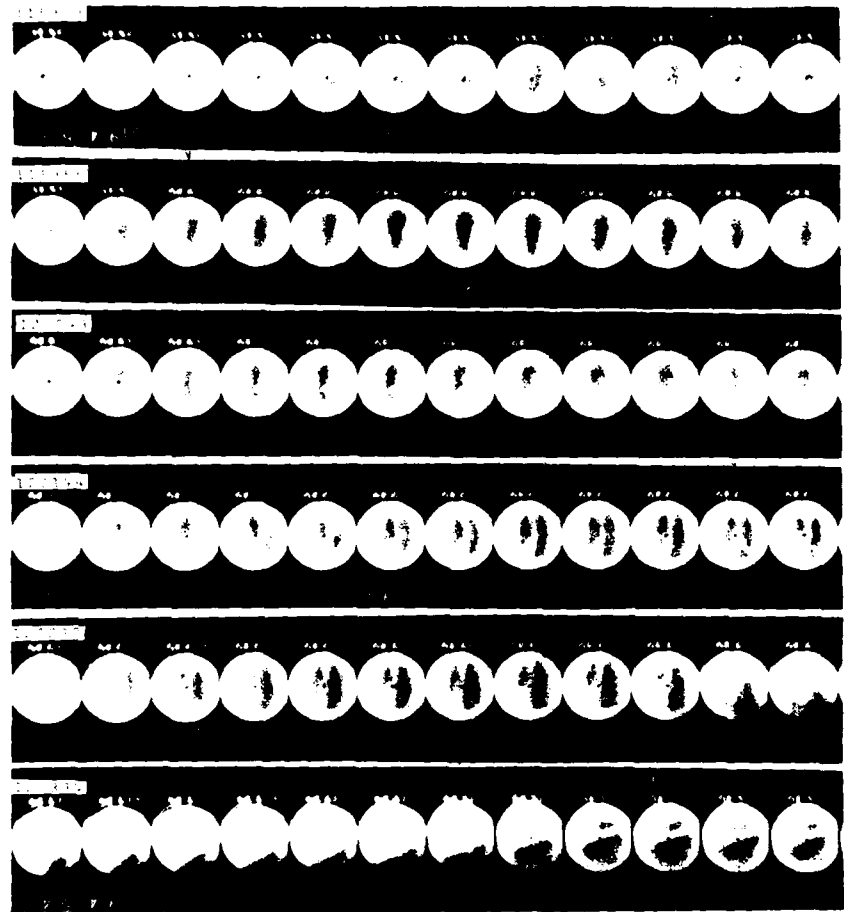


Figure A24. All-Sky Photographs for Case 13, Flight 026, 18 August 1980

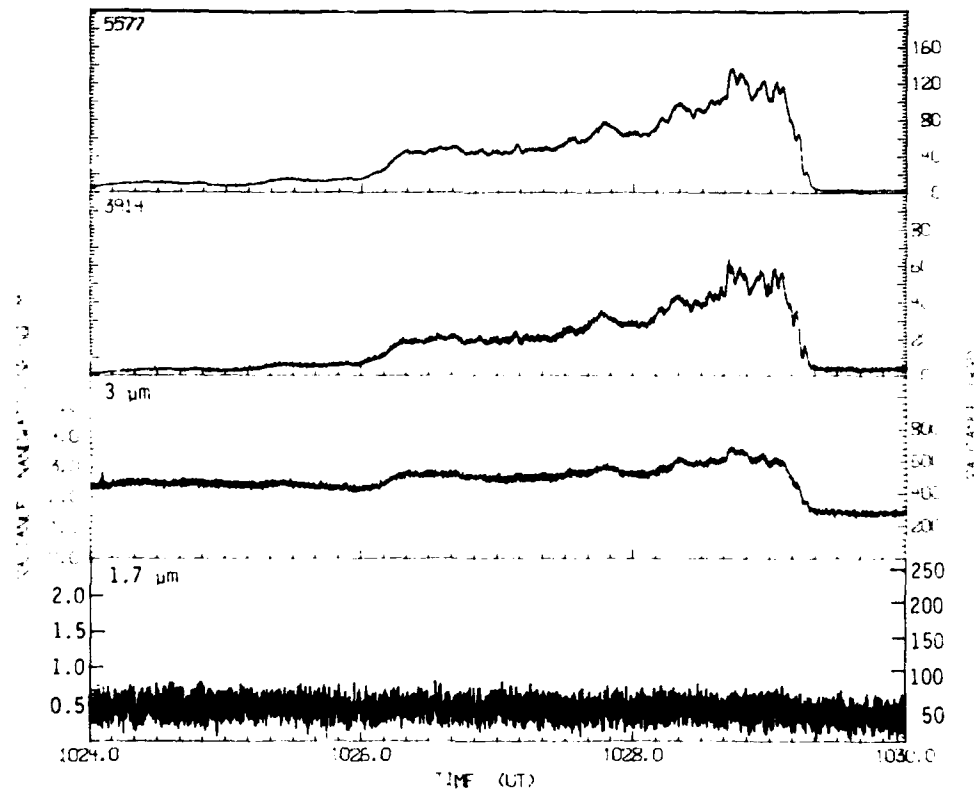


Figure A25. Case 14, Flight 027, 19 August 1980

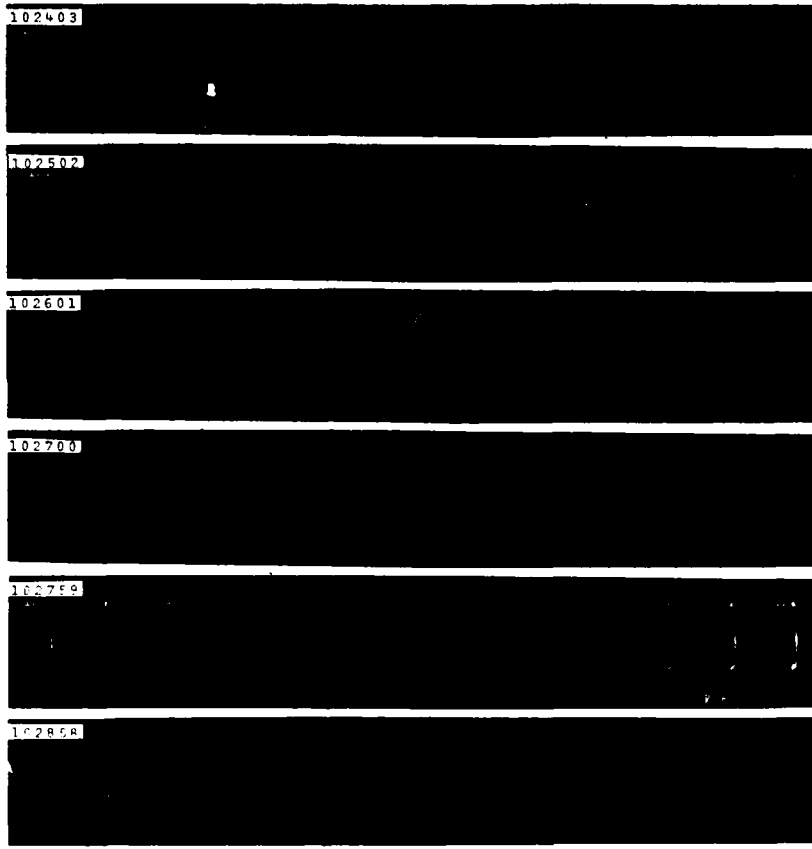


Figure A26. All-Sky Photographs for Case 14, Flight 027, 19 August 1980

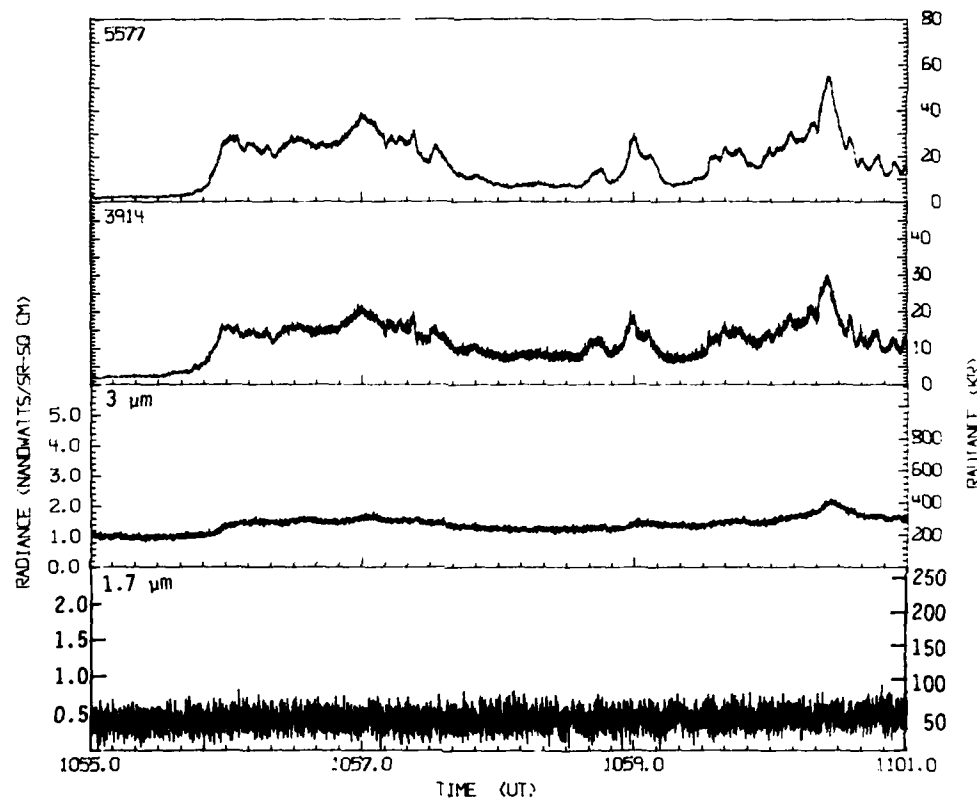


Figure A27. Case 15A, Flight 027, 19 August 1980

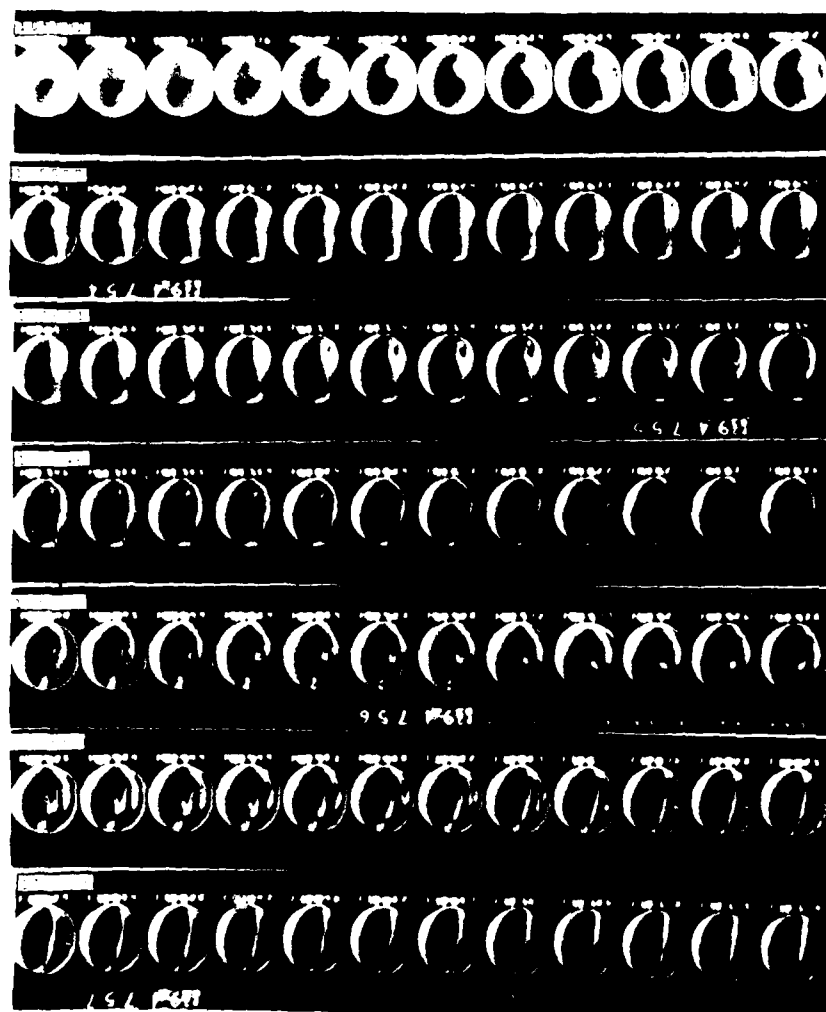


Figure A28. All-Sky Photographs for Case 15A, Flight 027, 19 August 1980

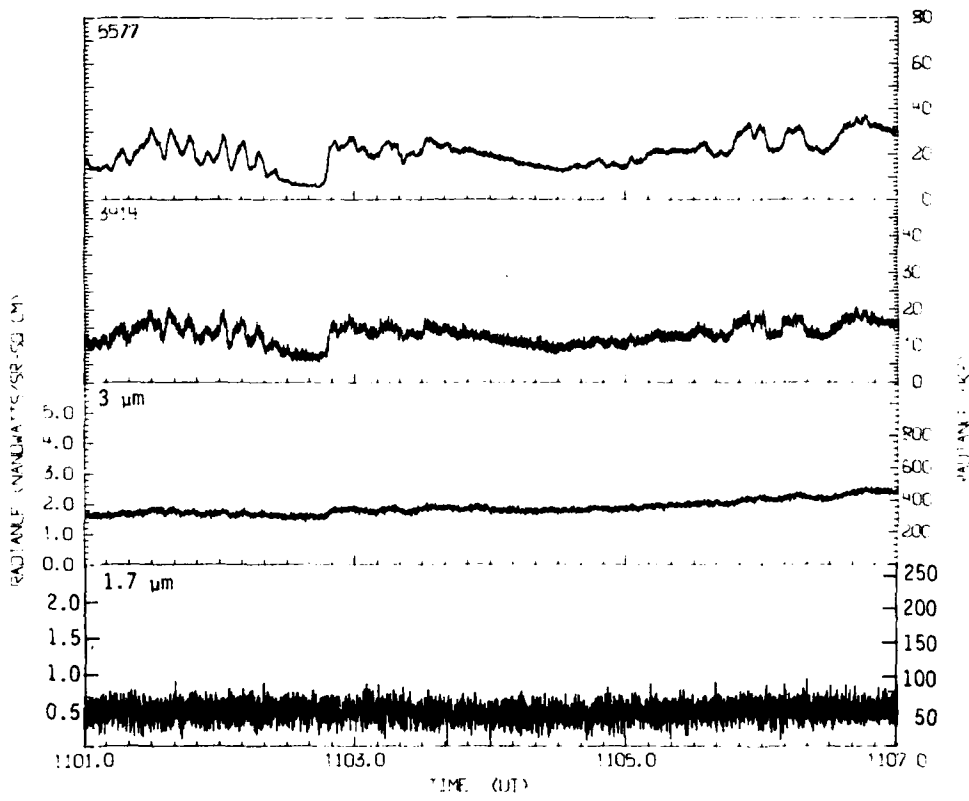


Figure A29. Case 15B, Flight 027, 19 August 1980

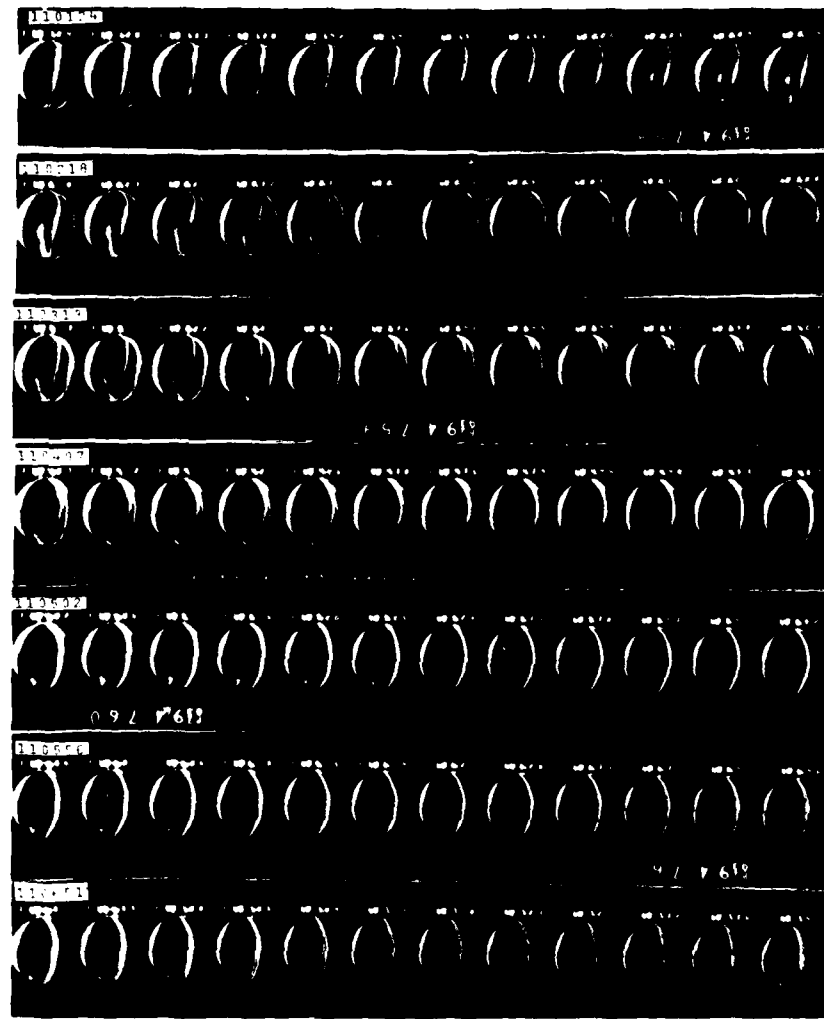


Figure A30. All-Sky Photographs for Case 15B, Flight 027, 19 August 1980

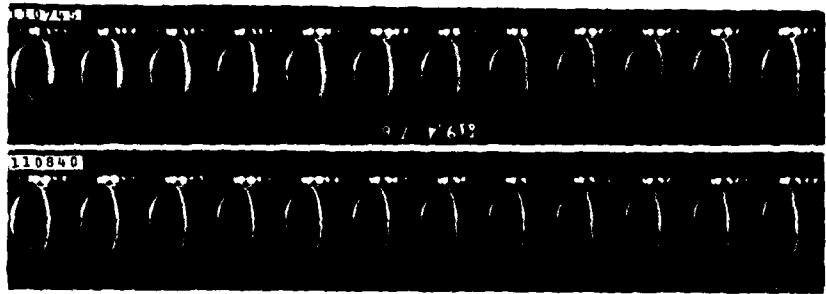


Figure A30. All-Sky Photographs for Case 15B, Flight 027, 19 August
1980 (Cont.)

Distribution List

Air Force Geophysics Laboratory
(AFGL)

Hanscom AFB, MA 01731

Attn: R. Nadile
R. O'Neil
R. Philbrick
B. Sandford
R. Sharma
A. T. Stair
J. Garing

Air Force Office of Scientific
Research (AFOSR)

Bolling, AFB, Washington D.C. 20332

Attn: D. Ball
T. Cress

Air Force Space Division/YL

P.O. Box 92960
Worldway Postal Center
Los Angeles, CA 90009

Attn: Col T. J. Cody
Lt Col O'Bryan
Lt G. Frantom

Air Force Technical Applications
Center (AFTAC)

Patrick AFB, FL 32925
Attn: Col R. Bigoni

Air Force Weapons Laboratory
(AFWL)

Kirtland AFB, NM 87117
Attn: Col J. Mayo

Defense Nuclear Agency
Washington D.C. 20305

Attn: Dr. H.C. Fitz
P. Lunn
Lt Col W. McKechnie

Aerospace Corporation
P.O. Box 92957
Los Angeles, CA 90009

Attn: J. Crestwell
P. Kisliuk
F. Simmons
T. Stocker
I. Spiro

Electro-Dynamics Laboratory
Utah State University
Logan, UT 84322

Attn: D. Baker
A. Steed

General Research Corporation
Santa Barbara, CA 93111
Attn: J. Ise

Kaman Nuclear Tempo
816 State Street (PO Drawer QQ)
Santa Barbara, CA 93102
Attn: T. Stephens

Lockheed Missiles and Space Co., Inc.
3251 Hanover Street
Palo Alto, CA 94304
Attn: J. Kumer
R. Sears

Mission Research Corporation
P.O. Drawer 719
Santa Barbara, CA 93102
Attn: D. Archer
D. Sappenfield

PhotoMetrics, Inc.
7 Arrow Way
Woburn, MA 01801
Attn: G. Davidson
I. Kolsky

Physical Sciences, Inc.
30 Commerce Way
Woburn, MA 01801
Attn: G. Caledonia

R&D Associates
P.O. Box 9695
Marina Del Ray, CA 90291
Attn: F. Gilmore
H. Mitchell

Space Measurements Laboratory
Utah State University
Logan, UT 84322
Attn: K. Baker
D. Burt

Space Data Corporation
1333 West 21st Street
Tempe, AZ 85282
Attn: S. Fisher
D. Kush

Stewart Radiance Laboratory
Utah State University
139 The Great Road
Bedford, MA 01730
Attn: R. Huppi
J. Ulwick

SRI International
333 Ravenswood Avenue
Menlo Park, CA 94025
Attn: W. Chestnut

Visidyne, Inc.
5 Corporate Place
S. Bedford Street
Burlington, MA 01803
Attn: J. Carpenter
T. Degges
C. Humphrey
W. Reidy
H. Smith

